Official journal of the CIOMP 2047-7538
www.nature.com/lsa

ARTICLE Open Access

Transient measurement of phononic states with covariance-based stochastic spectroscopy

Giorgia Sparapassi[1,2], Stefano M. Cavaletto[3], Jonathan Tollerud[4]✉, Angela Montanaro[1,2], Filippo Glerean[1,2], Alexandre Marciniak[1,2], Fancesca Giusti[1,2], Shaul Mukamel[3] and Daniele Fausti[1,2]✉

Abstract

We present a novel approach to transient Raman spectroscopy, which combines stochastic probe pulses and a covariance-based detection to measure stimulated Raman signals in alpha-quartz. A coherent broadband pump is used to simultaneously impulsively excite a range of different phonon modes, and the phase, amplitude, and energy of each mode are independently recovered as a function of the pump–probe delay by a noisy-probe and covariance-based analysis. Our experimental results and the associated theoretical description demonstrate the feasibility of 2D-Raman experiments based on the stochastic-probe schemes, with new capabilities not available in equivalent mean-value-based 2D-Raman techniques. This work unlocks the gate for nonlinear spectroscopies to capitalize on the information hidden within the noise and overlooked by a mean-value analysis.

Introduction

Nonlinear optics represents an active research field, dealing with phenomena occurring when intense light interacts with a material. This field is advanced by frequent technological and theoretical developments, delivering a deeper understanding of the properties of matter and revealing delicate interplays between different degrees of freedom. For instance, time-resolved spectroscopies such as Raman scattering techniques employ pairs of ultrashort pulses to track the dynamics of transient photo-induced electronic states[1–3]. Tailored time or wavevector combinations of multiple pulses are employed to extract specific nonlinear responses from a sample in multi-dimensional spectroscopy, a powerful nonlinear technique exploring the complex energy landscape of biological samples[4,5], quantum wells[6], or polymers[7].

However, nonlinear optical techniques rely on extremely weak signals, often orders of magnitude weaker than the linear response[8]. This challenge has been circumvented largely by creative signal-isolation strategies[9–12] and advancements in mathematical descriptions of nonlinear signals[8,13]. It has also been enabled by extensive effort and investment in stable laser systems and experimental set-ups[9]. Most experimental techniques rely on this stability and a mean-value analysis framework, in which the signal is measured in an integrated fashion (e.g. at the detector level or through repeated measurements) to reduce the noise until a suitable signal-to-noise ratio is achieved.

This approach has some drawbacks. Higher-order measurements become increasingly challenging due to the rapid diminishment of the signal efficiency, making anything beyond 5th-order experimentally impractical in many cases. In certain contexts, this is quite limiting. For example, techniques aiming to measure a Raman-echo (the Raman equivalent of photon-echo[14,15] and spin-echo[16] techniques which have proven extremely effective for multidimensional spectroscopy at IR/optical[4,9,17,18] and radio frequencies[19,20], respectively) attracted significant effort in the 90's and early 2000's but have not seen widespread adoption due to the requirement of 7th-order signal[21–23]. 5th-order 2D-Raman equivalents have been developed and remain an active area of research

Correspondence: Jonathan Tollerud (jtollerud@swin.edu.au) or Daniele Fausti (daniele.fausti@elettra.eu)
[1]Physics Department, University of Trieste, Trieste, Italy
[2]Elettra-Sincrotrone Trieste S.C.p.A., Trieste, Italy
Full list of author information is available at the end of the article

even though they only provide a subset of the capabilities of a 7th-order Raman echo technique[24–29].

The mean-value detection is intrinsically blind to the information contained in the noise. We have previously demonstrated a paradigmatically different framework in which the noise is seen as an asset rather than a liability in order to access information the mean-value misses[30], and similar schemes have also recently been reported[31,32]. In our initial demonstration, we resolved the impulsive-stimulated Raman scattering (ISRS) spectrum of quartz using a single-beam experiment. The nonlinear interaction of noisy input pulses with the Raman-active modes in the quartz generated spectral correlations that we resolved through a covariance-based analysis technique.

In this work, we apply the same covariance-based analysis framework to a transient ISRS measurement. Unlike traditional mean-value-based ISRS measurements[33,34], the covariance-based framework allows us to resolve the phase, amplitude, and frequency of each mode excited impulsively by the broadband coherent pump pulse for each pump–probe delay. We can thus clearly separate contributions from different modes and identify signals even when many modes are simultaneously excited by the pump.

The measurement is well described by a 3rd-order time-resolved ISRS model, where we fully account for the correlation properties of the stochastic probe pulse used. The model recovers the experimental features observed, and fully supports our interpretation of the signal in this novel configuration.

In addition to improving upon mean-value-based ISRS techniques, this correlation-based experimental framework could be extended to 5th-order by adding a second pump pulse to perform a 2D Raman measurement. Compared with current techniques, this would provide additional insight by spectrally resolving the energy of the final interaction[28,34,35] and could be used to measure spectral diffusion and population dynamics which in a mean-value-based framework require a 7th-order experiment. Our proof-of-principle results and theory supporting them demonstrate the feasibility of such a measurement.

Results

In a previous single-beam experiment, we showed that a broadband pulse with a stochastic spectral phase can resolve Raman spectra through a correlation-based analysis of pulse-to-pulse intensity fluctuations[30]. In this framework, the nonlinear response of the sample is imprinted in the intensity distribution, in the form of a statistical correlation between different frequencies in the transmitted pulse spectrum. A correlation develops when the frequency difference of two spectral components within the pulse spectral bandwidth matches the low-energy vibrational levels of the crystal. A Raman spectrum can thus be extracted from the statistical distribution of the frequency-resolved intensity.

Here, we combine the stochastic probe with a spectrally coherent pump pulse to study transient ISRS in α-quartz with a correlation-based measurement as depicted in Fig. 1a. As shown in Fig. 1b, the probe pulse is randomized on a single-shot basis using a diffraction-based pulse shaper, and the transmitted spectrum of thousands of unique pulses is acquired for each pump–probe time delay Δt. Mean-value detection completely overlooks the information in the probe pulse, because the stochastic transmitted spectra average out to zero. To retrieve information, we thus exploit a covariance-based analysis and calculate the Pearson correlation (the covariance over multiple repeated measurements divided by the standard deviation) of the spectrally resolved intensity of the transmitted pulse $I_{\mathrm{OUT}}(\omega_{\mathrm{OUT}})$ with a reference pulse $I_{\mathrm{IN}}(\omega_{\mathrm{IN}})$ routed around the sample. In this context, the Pearson coefficient quantifies the degree to which a stochastic intensity fluctuation at ω_{IN} induces a separate intensity fluctuation at ω_{OUT} through the nonlinear ISRS interaction of the light with the sample. This calculation is repeated for all combinations of ω_{OUT} and ω_{IN}, resulting in a three-dimensional matrix $\rho_c(\omega_{\mathrm{IN}}, \omega_{\mathrm{OUT}}, \Delta t)$, from which we can extract spectrally and temporally resolved information. The correlation properties of the stochastic probe pulses used in the experiment are described in the Supplementary Information (SI). The time profile of a randomized pulse contains a strong central spike, whose width is comparable to the pristine laser pulse duration, and a noisy tail contributed by the added spectral noise. The short coherent spike dictates the time resolution of the experiment, which can resolve the coherent evolution of the phonon even with long noisy tails (>1 ps). We introduce the stochastic phase on the high-energy side of the pulse (>368 THz), while leaving lower frequencies noise free, providing a reference field for self-heterodyne measurement of the signal. We will focus on the lower right quadrant (indicated by the dashed black box in Fig. 1c) which is most sensitive to signals that appear for ω_{OUT} and ω_{IN} below and above 368 THz, respectively.

In this quadrant the transmitted probe is stochastic, but the reference is not and the ISRS signal produces a uniform diagonal feature for each mode that is shifted away from the $\omega_{\mathrm{IN}} = \omega_{\mathrm{OUT}}$ diagonal by the phonon frequency. We thus introduce the Raman frequency $\omega_{\mathrm{R}} = \omega_{\mathrm{OUT}} - \omega_{\mathrm{IN}}$, redefine our frequency axes as ω_{OUT} and ω_{R}, and then transform the data onto this new grid by shifting each row by ω_{OUT} such that the diagonal features of unitary slope become vertical lines. We then project the resulting 2D array onto the ω_{R} axis by integrating across ω_{OUT} (as shown in Fig. 1c–f). This compresses each correlation map into a single one-dimensional array which can be

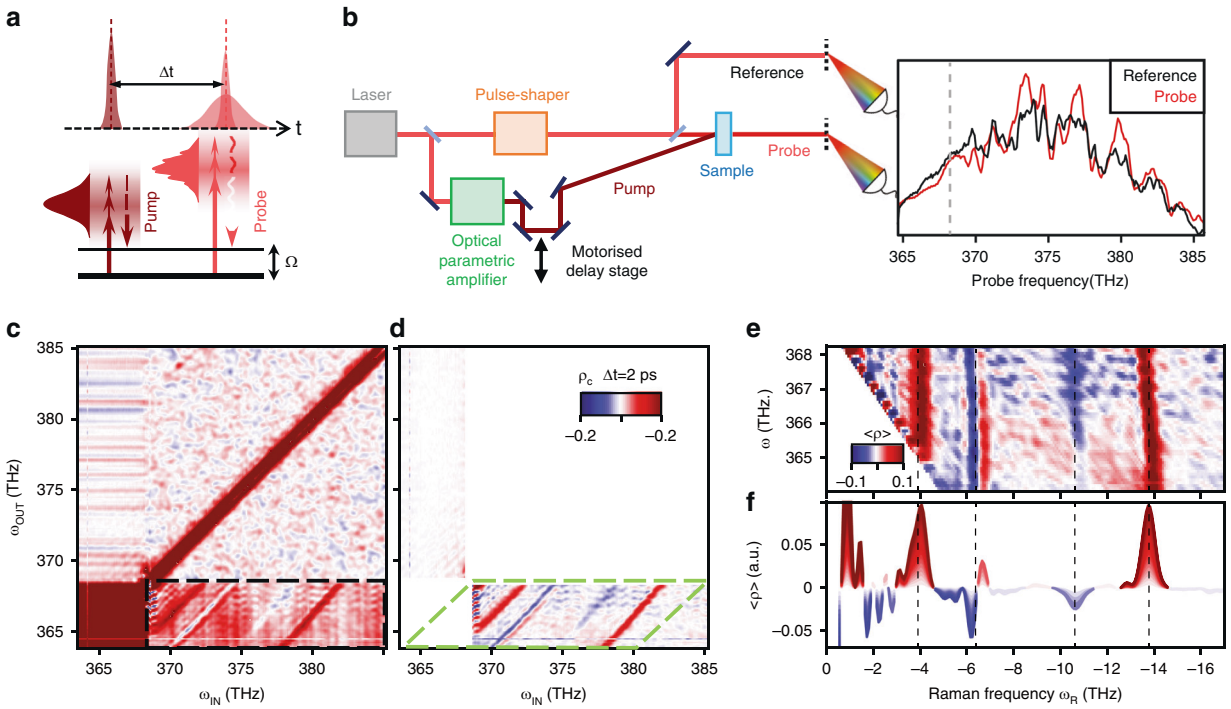

Fig. 1 Impulsive Stimulated Raman Signal (ISRS) in covariance-based pump–probe. a Diagram of the ISRS interaction. **b** Time-domain representation of the experiment. Spectra of the probe (red) and reference (black) are recorded at each time delay Δt and used to calculate the spectrally resolved correlation coefficient ρ_c. The vertical grey line indicates the cut-off frequency above which uncorrelated noise was introduced. Pseudo-colormaps of ρ_c for $\Delta t = 2$ ps **c** as measured and **d** after subtracting the median in the lower-right and upper-left quadrant for each ω_{IN} and ω_{OUT} (respectively). **e** The block within the dashed green line in **d** is recast by shifting each row from **d** by ω_{OUT} and plotted as a function of the frequency difference ω_R. **f** The matrix in **e** is averaged over ω_{OUT} yielding $<\rho_c(\omega_R)>$. Black dashed vertical lines indicate the frequency of known Raman modes of quartz.

conveniently plotted and analysed as a function of the pump–probe delay Δt. The result is a two-dimensional map $<\rho_c(\omega_R, \Delta t)>$

$\rho_c(\omega_{IN}, \omega_{OUT})$ maps for selected delays are shown in Fig. 2a. The ISRS signal emerges after the pump excitation as diagonal stripes of nonzero correlation, whose sign evolves with the time delay. Each map is integrated as described above, to produce a single one-dimensional array for each time delay (see Fig. 2b) and stacked horizontally to build the frequency vs. time $<\rho_c(\omega_R, \Delta t)>$ map (see Fig. 2c), that shows the time evolution of the multimode correlation signal. The ISRS signal thus appears as a narrow feature in ω_R that oscillates as a function of Δt, and which overlaps a "coherent artefact"-like signal[36,37] at short times (the coherent artefact is described below).

A Hilbert transformation is applied as a function of ω_R to rotate the phase of the real-valued $<\rho_c(\omega_R, \Delta t)>$ yielding a complex-valued dataset. A Fourier transform is then applied as a function of Δt, resulting in a frequency–frequency map (see Fig. 2d) with the new axis $\omega_{\Delta t}$. In the $<\rho_c(\omega_R, \omega_{\Delta t})>$ map (referred to as a 2D spectrum), we find the phonon spectrum along the vertical axis, and the frequency of oscillations along the horizontal axis. The probe interaction with the active vibrations gives rise to peaks in the 2D spectrum, located at $\omega_{\Delta t} = \pm\omega_R = \pm\Omega$ for each mode Ω of α-quartz. The frequency of known vibrational modes in quartz are indicated by the horizontal dashed lines. This 2D spectrum is obtained scanning only one inter-pulse delay and exploiting the correlation over the broad bandwidth of the randomized probe pulse to monitor the Raman mode directly. The dephasing rate and the energy of the modes are apparent in the FFT width and position, respectively.

When the pulses temporally overlap ($|\Delta t|<1.5$ ps), the pulse ordering is undetermined and additional signals overlap the ISRS signal of interest. This effect (often referred to as a coherent artefact or cross-phase modulation) results in a symmetrical signal along Δt[38] (as can be seen in Fig. 2c) made up of fringes across the spectrum whose periodicity decreases with an increasing $|\Delta t|$. The resulting correlation is an oscillating background, whose fronts are parallel to the correlation-map diagonal (as can be seen in Fig. 2a, −1 ps). In the $<\rho_c(\omega_R, \Delta t)>$ map, this overlap signal resembles a hyperbola, centred at the axes' origin (as can be seen in Fig. 2c). In the 2D spectrum $<\rho_c(\omega_R, \omega_{\Delta t})>$, this is a diagonal feature along the $\omega_R \pm \omega_{\Delta t}$ lines (as can be seen in Fig. 2d).

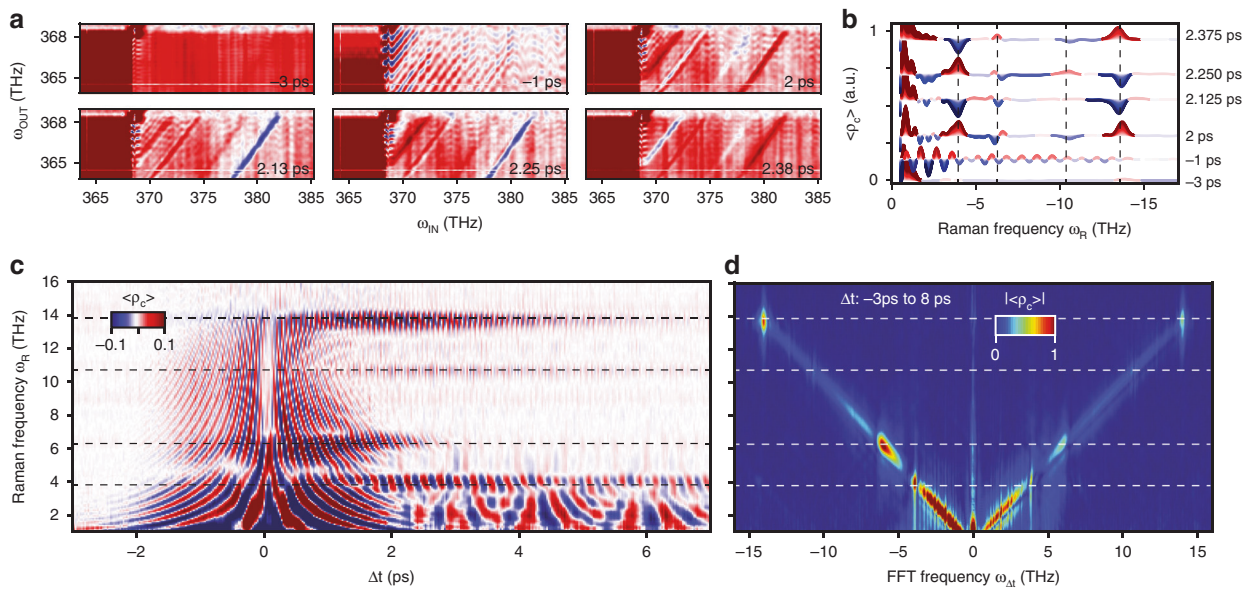

Fig. 2 Time evolution of the ISRS signal. a ρ_c (ω_{IN}, ω_{OUT}) and **b** <ρ_c(ω_R)> for selected values of the time delay Δt, showing the sign evolution of the vibrational signal. **c** Pseudo-colormap of <ρ_c (ω_R, Δt)>. **d** 2D ISRS spectrum, achieved by Hilbert and Fourier transforms of <ρ_c (ω_R, Δt)> as a function of ω_R and Δt, respectively. Vertical (horizontal) dashed lines in **b** (**c**, **d**) indicate the frequency of known Raman modes of quartz.

The experiment is well described by a 3rd-order model reported in detail in the SI. The double manifold representing the sample is coupled by the pulse electric fields inducing an electronically off-resonant Raman process[13]. Pairs of interactions within the pump spectrum, at frequencies whose difference matches the vibrational energy, create a coherent superposition of vibrational states. The coherence evolves over the pump–probe time delay Δt and is monitored by a subsequent off-resonant Raman excitation involving two interactions with the stochastic probe pulse. The resulting ISRS signal, obtained by frequency dispersing the transmitted probe pulse at varying pump–probe time delays, features Stokes- and anti-Stokes-type contributions, with time-delay-dependent oscillations resulting from the phase of the coherence encountered by the probe pulse[39,40]. The covariance signal, given by products of IN and OUT pulse intensities and thus involving four interactions with the stochastic probe pulse, is calculated in terms of the two- and four-point field correlation functions, taking into account the peculiar stochastic properties of the pulses generated in the experiment and the impact of the gating performed by the discrete detector array.

The calculated 2D ISRS spectrum for the phonon frequencies involved in the experiment is shown in Fig. 3. Here, the diagonal contributions stemming from overlapping pump and probe pulses are added to the ISRS signal. The measured spectrum in Fig. 2d is mostly reproduced by the model as shown in Fig. 3. However, the different peak amplitude of the 6 THz phonon in the two

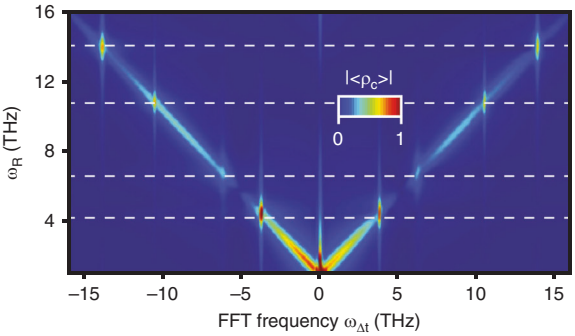

Fig. 3 Simulated ISRS spectrum using the model described in the main text and Supplementary Information. Horizontal lines indicate the frequency of known Raman modes of quartz.

quadrants of the experimental 2D ISRS spectrum is not captured in the 3rd-order model, pointing at higher-order contributions, such as a phonon-phonon coupling[41].

Phonon dephasing times can be extracted by fitting the phonon linewidth in the $\omega_{\Delta t}$ domain or by fitting the exponential decay in the Δt domain. We fit the three most prominent phonon features (3.9 THz, 6.2 THz, 13.9 THz) in Δt domain and compared the dephasing times extracted using traditional mean-value-based pump–probe spectroscopy (see SI for details). We found that the dephasing times measured using the covariance-based and mean-value-based approaches were in good agreement.

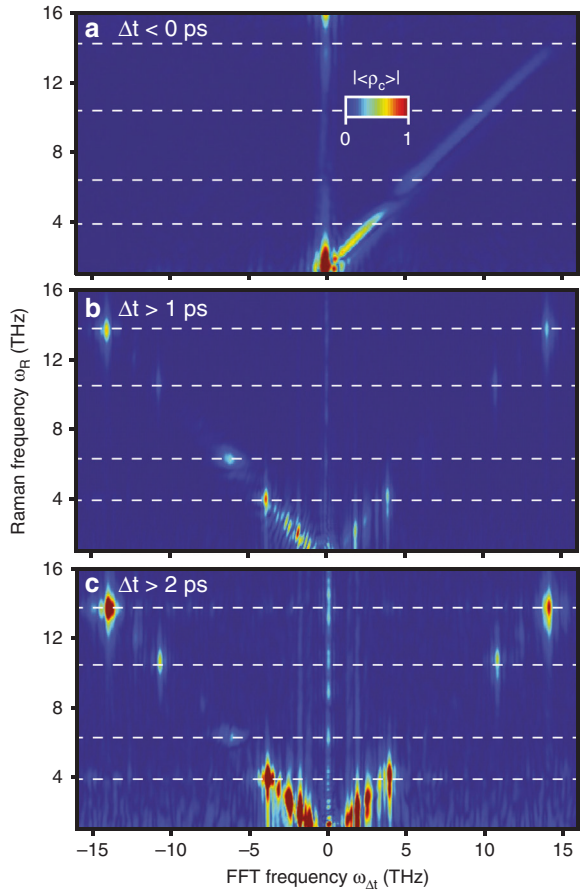

Fig. 4 Different contributions to the ISRS signal can be resolved depending on how the data is windowed in the time domain, Δ*t*. **a** When selecting the negative time delays, the only contribution to the 2D spectrum is the 1:1 diagonal. When the pump–probe overlap is **b** partially and **c** fully excluded, the overlap diagonals are reduced and fully removed (respectively), leaving only discrete ISRS peaks. Horizontal lines indicate the frequency of known Raman modes of quartz.

One challenge with this technique is to separate the ISRS from the coherent-artefact signal, which overlaps the Raman modes in the 2D spectrum and partially in $<\rho_c(\omega_R, \Delta t)>$. One way to separate these two contributions is by applying a window function in the time domain. This can be seen in Fig. 4, where multiple window functions have been applied to separate the different contributions. Clearly, removing the entire 2 ps overlap is not suitable for modes with short dephasing times (e.g. the 6 THz mode). The duration of the noisy tails in the probe pulse is inversely proportional to the correlation length of the stochastic probe phase, so the length of the pump–probe overlap signal can also be reduced, but at the cost of diminished spectral resolution. In practice, an optimal correlation length would be chosen by balancing these two factors based on the needs of the experiment.

The spectrally uncorrelated fluctuations in the probe pulses are critical to the functionality of this experiment, but uncorrelated noise from other sources has a detrimental effect and may hide the presence of the correlations induced by the sample. The primary source of this unwanted spectrally uncorrelated noise is in the detection system, which generates a 'white' noise spread across the covariance maps. Through an analysis provided in the SI, we show that this uncorrelated noise is at least an order of magnitude below the peak signal for most of the observed phonon modes, and can be reduced by increasing the number of unique phase patterns applied to the probe pulse for each time delay.

Discussion

The ability to resolve the energy of the Raman modes is undoubtedly a strength of this correlation-based framework compared with mean-value ISRS, but the ability to track the phase of the mode as a function of the pump–probe delay is also useful. First, this phase evolution provides a "sanity-check", as the frequency of the mode generated in the final state must match the frequency of the oscillations in the pump–probe time delay, but it also enables separating the signal along two different frequency axes, so overlapping signals (such as closely spaced modes) are more readily distinguished. This can be seen especially clearly in the low-energy modes in Fig. 4c, which cannot be easily separated in the correlation maps alone.

We observe different amplitudes of the Raman peaks for positive and negative $\omega_{\Delta t}$, even when taking into account the overlap signal. This is in contrast with the theory, which predicts symmetric spectral amplitudes. The most apparent mismatch is found in correspondence of the combination signals involving the 6 THz phonon. This discrepancy could be due to a higher-order coupling to other elementary excitations in the sample, possibly a beating resulting from an anharmonic interaction[42–44], or to a nontrivial decay channel for the aforementioned phonon[45], which is the widest (and one of the most intense) of those within the probe spectral bandwidth.

It is well known that a 3rd-order measurement does not contain information on the pure decoherence of the vibrational modes, and that a 7th-order measurement (with four pairs of light–matter interactions) is required to measure the Raman equivalent of 2D-IR photon-echo experiments (typically referred to as a Raman-echo). The success of 2D-IR (and analogues in RF and the visible) suggests that such a Raman-echo experiment would provide very useful information, but it is experimentally challenging to the point of impracticality. As such, 5th-order Raman experiments (typically referred to as 2D-Raman) have been developed and can access some of the same information, but importantly, they lack sensitivity to

population dynamics that have made the equivalent 2D-IR techniques so effective[28,35].

A 5th-order 2D-Raman measurement with covariance-based detection would have some key advantages over mean-value-based techniques. It is intrinsically sensitive to weak signals, because even a small signal can generate a strong correlation. Being able to resolve the phase and energy of the final interaction will enable new ways to separate 5th-order signals from 3rd-order cascades, which is a common challenge in 2D Raman[46,47]. Finally, we expect that it will enable fast measurement of 2D spectra because only a single delay needs to be scanned, unlike current techniques which require scanning of two delays.

More importantly, 5th-order 2D-Raman with covariance-based detection will enable measurement of some population signals, which is not possible in current mean-value based techniques. The capability of the covariance-based detection to resolve the energy of the final state is functionally analogous (albeit imperfectly) to the role of spectrally resolved or time-resolved heterodyne detection in 2D-IR and 2D electronic spectroscopy, which are phase-resolved photon echo techniques requiring three characteristic time domains[9,10,20]. The state of the system during two of the time domains is determined by scanning the two inter-pulse delays while tracking the phase of the signal, but the state of the system in the third time period after the final interaction (which is critical for capturing the photon echo) is determined by interference between the signal and a reference field. Without this heterodyne detection scheme, a fourth excitation pulse is needed to probe the system and resolve the dynamics in this final time delay[10].

In a Raman-echo measurement, each of these interactions is doubled, so four pairs of interactions are required to generate the three characteristic time periods[34]. However, the covariance-based detection allows us to infer the state of our system in the final time period through the correlations induced in the probe pulse by the final Raman interaction. We can then generate a non-rephasing 2D-spectrum in which one axis is the inferred state of the system in the final time domain (measured through the spectral correlations in the probe) and the other is the state of the system in the first time domain (the phase evolution of the spectral correlations as a function of the inter-pulse delay). The population dynamics of the non-rephasing signals could then be probed by collecting 2D spectra as a function of the second time delay. Importantly, there is no access to rephasing pathways (and thus no separation of homogeneous and inhomogeneous broadening) because the inference will only provide the state of the system immediately after the final interaction, whereas the Raman echo will form subsequently in inhomogeneously broadened modes. Still, this access to the population dynamics would be a powerful new additional capability not possible in current 2D Raman techniques.

In conclusion, we have shown that the signal from low-energy excitations of a crystalline sample can be mapped within a time-resolved spectroscopic experiment by use of a single delay line in conjunction with a spectrally randomized probe. In this framework, the energy, phase, and amplitude of each Raman mode can be read out directly through correlations in the spectrum of the optical probe pulse. The covariance-based signal measured is consistent with a theoretical model predicting that the oscillation frequency of the signals as a function of the pump–probe delay should match the frequencies of the signals in a covariance-based analysis of the probe spectra.

This work is a key step towards covariance-based 2D Raman spectroscopy—an alternative approach to 2D Raman using mean-value signal detection—which promises to decrease experimental complexity, reduce acquisition times, and enable new insights such as measurement of Raman coherence and population dynamics in a 5th-order experiment. More broadly, this work demonstrates the feasibility of a covariance-based framework in transient nonlinear spectroscopy and its advantages over mean-value-based approaches and will inspire similar efforts to utilize higher modes beyond the mean-value in other nonlinear techniques.

Our work demonstrates that covariance-based spectroscopy is a feasible and advantageous route to retrieve temporal and spectral resolution from stochastic probes. This is also relevant at hard-x-ray frequencies, where current x-ray free-electron lasers (FELs) based on the self-amplified spontaneous emission (SASE) mechanism generate intense pulses which are intrinsically stochastic[48,49]. Covariance-based signals have been used in theory and experimental investigations with stochastic FEL pulses[50–54], and were recently shown to provide the same temporal and spectral resolution as signals obtained by coherent pulses[55,56]. They thus represent an essential ingredient for the implementation of multidimensional nonlinear x-ray spectroscopy[57] with existing technology.

Materials and methods

The sample is an α-quartz crystal, with 1 mm thickness.

The laser employed in the experiments is a Coherent Legend Elite Duo, producing pulses at a repetition rate of 5 kHz, with wavelength $\lambda = 795$ nm, and duration 45 fs. The pump is collected with a window before the beam is sent through the pulse shaper. The wavelength of the pump is down-converted to $\lambda = 1300$ nm using a home-made double stage optical parametric amplifier. The pump has a duration of 110 fs (as measured with a homemade FROG system), and a fluence of 4.5 mJ/cm^2. The probe is routed into a diffraction-based liquid crystal spatial light modulator (Vaughan 2005), that randomizes

shot by shot its spectral phase. The resulting average probe pulse, in the time domain, is made of a central spike whose width is essentially untouched by the randomization, and a broad shoulder lasting roughly 1–1.5 ps.

The randomized beam is finally separated into a reference, selected before the sample, and a probe, transmitted by the sample, with 0.025 mJ/cm^2 fluence. The probe power is kept low enough that no features can be resolved in correlation maps in which the pump is blocked, so the detected signal is not contaminated by probe-only correlations. While this signal could also in principle result from scatter interference between pump and probe, we rule this out because of the wavelength difference.

A homemade detection system was used. It is composed of a pair of twin Hamamatsu photodiode arrays, triggered by the laser and at the same repetition rate, that digitize the dispersed probe and reference spectra. The actual experimental repetition rate is lowered by the slow rotation dynamics of the liquid crystals the pulse shaper is based on. The frequency resolution, roughly 0.2 THz, is determined by the narrow average width of the spiky spectral profile, in turn given by the random spectral phase correlation length.

We apply the following real-to-complex transformation to the frequency vs. time $<\rho_c(\omega_R, \Delta t)>$ map in order to remove the symmetry between the negative and positive Fourier frequency components in the 2D spectrum $<\rho_c(\omega_R, \omega_{\Delta t})>$. This also allows us to distinguish the overlap signal from the Raman signal, as the first is symmetrical around the pump–probe overlap along the time delay axis, while the latter is only present at positive time delays.

The data in $<\rho_c(\omega_R, \Delta t)>$ is Fourier transformed along the ω_R axis to produce a $<\rho_c(t_R, \Delta t)>$ time vs. time map. Only one half of this map is meaningful as the starting data is real valued. We window out the mirrored half and perform an inverse Fourier Transform along the Δt_R axis. The $<\rho_c(\omega_R, \Delta t)>$ map we obtain is complex valued, therefore its Fourier Transform along the true time delay axis is meaningful all along the $\omega_{\Delta t}$ axis, in other words the FT spectrum is not mirrored. Before performing this last FT though, we zero pad the time-dependent data in order to smooth its edges and remove any artifacts from the 2D spectrum. The procedure just outlined corresponds to performing the Hilbert transform of the signal.

Acknowledgements
This work was supported by the European Commission through the European Research Council (ERC) Starting Grant Project "Inhomogenieties and Fluctuations in Quantum Coherent Matter Phases by Ultrafast Optical Tomography (INCEPT)" (Grant#677488). DF aknowledges the support of ERC Proof of Concept grant COBRAS (Grant#860365). This work has been performed using the LEGEND laser source made available by the Nanoscience Foundry and Fine Analysis (NFFA-MIUR Italy Progetti Internazionali) facility. S.M.C. gratefully acknowledges the support of the Alexander von Humboldt foundation through the Feodor Lynen program. S.M.C. and S.M. gratefully acknowledge the support of the National Science Foundation (Grant CHE-1953045).

Author details
[1]Physics Department, University of Trieste, Trieste, Italy. [2]Elettra-Sincrotrone Trieste S.C.p.A., Trieste, Italy. [3]Department of Chemistry and Department of Physics & Astronomy, University of California, Irvine, CA, USA. [4]Optical Sciences Centre, Swinburne University, Melbourne, Australia

Conflict of interest
The authors declare no conflict of interest.

Supplementary information The online version contains supplementary material available at https://doi.org/10.1038/s41377-022-00727-6.

Received: 16 August 2021 Revised: 17 January 2022 Accepted: 26 January 2022
Published online: 01 March 2022

References

1. Yan, Y. X., Gamble, E. B. Jr. & Nelson, K. A. Impulsive stimulated scattering: general importance in femtosecond laser pulse interactions with matter, and spectroscopic applications. *J. Chem. Phys.* **83**, 5391–5399 (1985).
2. Weiner, A. M., Leaird, D., Wiederrecht, G. P. & Nelson, K. A. Femtosecond multiple-pulse impulsive stimulated Raman scattering spectroscopy. *JOSA B* **8**, 1264–1275 (1991).
3. Prince, R. C., Frontiera, R. R. & Potma, E. O. Stimulated Raman scattering: from bulk to nano. *Chem. Rev.* **117**, 5070–5094 (2017).
4. Hybl, J. D., Albrecht Ferro, A. & Jonas, D. M. Two-dimensional Fourier transform electronic spectroscopy. *J. Chem. Phys.* **115**, 6606–6622, https://doi.org/10.1063/1.1398579 (2001).
5. Cho, M. Coherent two-dimensional optical spectroscopy. *Chem. Rev.* **108**, 1331–1418 (2008).
6. Li, X., Zhang, T., Borca, C. N. & Cundiff, S. T. Many-body interactions in semiconductors probed by optical two-dimensional Fourier transform spectroscopy. *Phys. Rev. Lett.* **96**, 057406 (2006).
7. Collini, E. & Scholes, G. D. Coherent intrachain energy migration in a conjugated polymer at room temperature. *Science* **323**, 369–373 (2009).
8. Potma, E. O. & Mukamel, S. Theory of coherent raman scattering. *Coherent Raman Scattering Microscopy*, 3–42 (2012).
9. Tollerud, J. O. & Davis, J. A. Coherent multi-dimensional spectroscopy: experimental considerations, direct comparisons and new capabilities. *Prog. Quantum Electron.* **55**, 1–34, https://doi.org/10.1016/j.pquantelec.2017.07.001 (2017).
10. Nardin, G. et al. Multi-dimensional coherent optical spectroscopy of semiconductor nanostructures: collinear and non-collinear approaches. *J. Appl. Phys.* **117**, 112804, https://doi.org/10.1063/1.4913830 (2015).
11. Jakubczyk, T. et al. Radiatively limited dephasing and exciton dynamics in MoSe2 monolayers revealed with four-wave mixing microscopy. *Nano Lett.* **16**, 5333–5339, https://doi.org/10.1021/acs.nanolett.6b01060 (2016).
12. Bakulin, A. A., Silva, C. & Vella, E. Ultrafast spectroscopy with photocurrent detection: watching excitonic optoelectronic systems at work. *J. Phys. Chem. Lett.* **7**, 250–258, https://doi.org/10.1021/acs.jpclett.5b01955 (2016).
13. Mukamel, S. *Principles of nonlinear optical spectroscopy*. (Oxford University Press on Demand, 1999).
14. Abella, I. D., Kurnit, N. A. & Hartmann, S. R. Photon echoes. *Phys. Rev.* **141**, 391–406, https://doi.org/10.1103/physrev.141.391 (1966).
15. De Boeij, W. P., Pshenichnikov, M. S. & Wiersma, D. A. Ultrafast solvation dynamics explored by femtosecond photon echo spectroscopies. *Annu. Rev. Phys. Chem.* **49**, 99–123, https://doi.org/10.1146/annurev.physchem.49.1.99 (1998).
16. Hahn, E. L. Spin Echoes. *Phys. Rev.* **80**, 580–594, https://doi.org/10.1103/physrev.80.580 (1950).
17. Kuhs, C. T., Luther, B. M. & Krummel, A. T. Recent advances in 2D IR spectroscopy driven by advances in ultrafast technology. *IEEE J. Sel. Top. Quantum Electron.* **25**, 1–13, https://doi.org/10.1109/jstqe.2019.2900597 (2019).
18. Aue, W. P., Bartholdi, E. & Ernst, R. R. Two-dimensional spectroscopy. Application to nuclear magnetic resonance. *J. Chem. Phys.* **64**, 2229–2246, https://doi.org/10.1063/1.432450 (1976).

19. Schmidt-Rohr, K., Schmidt-Rohr, K. & Spiess, H. W. *Multidimensional Solid-State NMR and Polymers*. (Elsevier Science, 1994).
20. Zanni, M. T. & Hochstrasser, R. M. Two-dimensional infrared spectroscopy: a promising new method for the time resolution of structures. *Curr. Opin. Struct. Biol.* **11**, 516–522, https://doi.org/10.1016/s0959-440x(00)00243-8 (2001).
21. Loring, R. F. & Mukamel, S. Selectivity in coherent transient Raman measurements of vibrational dephasing in liquids. *J. Chem. Phys.* **83**, 2116–2128, https://doi.org/10.1063/1.449302 (1985).
22. Bout, D. V., Freitas, J. E. & Berg, M. Rapid, homogeneous vibrational dephasing in ethanol at low temperatures determined by Raman echo measurements. *Chem. Phys. Lett.* **229**, 87–92, https://doi.org/10.1016/0009-2614(94)01013-7 (1994).
23. Inaba, R., Tominaga, K., Tasumi, M., Nelson, K. A. & Yoshihara, K. Observation of homogeneous vibrational dephasing in benzonitrile by ultrafast Raman echoes. *Chem. Phys. Lett.* **211**, 183, https://doi.org/10.1016/0009-2614(93)85183-o (1993).
24. Tanimura, Y. & Mukamel, S. Two-dimensional femtosecond vibrational spectroscopy of liquids. *J. Chem. Phys.* **99**, 9496–9511, https://doi.org/10.1063/1.465484 (1993).
25. Guo, Z., Molesky, B. P., Cheshire, T. P. & Moran, A. M. Elucidation of reactive wavepackets by two-dimensional resonance Raman spectroscopy. *J. Chem. Phys.* **143**, 124202, https://doi.org/10.1063/1.4931473 (2015).
26. Molesky, B. P., Giokas, P. G., Guo, Z. & Moran, A. M. Multidimensional resonance Raman spectroscopy by six-wave mixing in the deep UV. *J. Chem. Phys.* **141**, 114202, https://doi.org/10.1063/1.4894846 (2014).
27. Guo, Z., Molesky, B. P., Cheshire, T. P. & Moran, A. M. Two-dimensional resonance Raman signatures of vibronic coherence transfer in chemical reactions. *Top. Curr. Chem.* **375**, https://doi.org/10.1007/s41061-017-0173-0 (2017).
28. Molesky, B. P., Guo, Z., Cheshire, T. P. & Moran, A. M. Perspective: two-dimensional resonance Raman spectroscopy. *J. Chem. Phys.* **145**, 180901, https://doi.org/10.1063/1.4966194 (2016).
29. Kuramochi, H., Takeuchi, S., Kamikubo, H., Kataoka, M. & Tahara, T. Fifth-order time-domain Raman spectroscopy of photoactive yellow protein for visualizing vibrational coupling in its excited state. *Sci. Adv.* **5**, eaau4490, https://doi.org/10.1126/sciadv.aau4490 (2019).
30. Tollerud, J. O. et al. Femtosecond covariance spectroscopy. *Proc. Natl Acad. Sci. USA* **116**, 5383–5386, https://doi.org/10.1073/pnas.1821048116 (2019).
31. Smith, R. P., Martin, E. W., Kira, M. & Cundiff, S. T. Toward direct optical excitation of excitonic many-body effects using intense thermal states. *OSA Contin.* **3**, 1283–1301, https://doi.org/10.1364/OSAC.392972 (2020).
32. Suresh, M. I., Russell, P. S. J. & Tani, F. Covariance spectroscopy of molecular gases using fs pulse bursts created by modulational instability in gas-filled hollow-core fiber. *Opt. Express* **28**, 34328–34336, https://doi.org/10.1364/OE.405767 (2020).
33. Laubereau, A. & Kaiser, W. Vibrational dynamics of liquids and solids investigated by picosecond light pulses. *Rev. Mod. Phys.* **50**, 607–665, https://doi.org/10.1103/revmodphys.50.607 (1978).
34. Fayer, M. D. *Ultrafast Infrared And Raman Spectroscopy*. (Taylor & Francis, 2001).
35. Kubarych, K. J., Milne, C. J. & Miller, R. J. D. Fifth-order two-dimensional Raman spectroscopy: a new direct probe of the liquid state. *Int. Rev. Phys. Chem.* **22**, 497–532, https://doi.org/10.1080/0144235031000121544 (2003).
36. Hamm, P. Coherent effects in femtosecond infrared spectroscopy. *Chem. Phys.* **200**, 415–429, https://doi.org/10.1016/0301-0104(95)00262-6 (1995).
37. Vardeny, Z. & Tauc, J. Picosecond coherence coupling in the pump and probe technique. *Opt. Commun.* **39**, 396–400, https://doi.org/10.1016/0030-4018(81)90231-5 (1981).
38. Fumero, G., Batignani, G., Dorfman, K. E., Mukamel, S. & Scopigno, T. On the resolution limit of femtosecond stimulated raman spectroscopy: modelling fifth-order signals with overlapping pulses. *ChemPhysChem* **16**, 3438–3443, https://doi.org/10.1002/cphc.201500548 (2015).
39. Dorfman, K. E., Fingerhut, B. P. & Mukamel, S. Time-resolved broadband Raman spectroscopies: a unified six-wave-mixing representation. *J. Chem. Phys.* **139**, 124113 (2013).
40. Batignani, G. et al. Genuine dynamics vs cross phase modulation artifacts in femtosecond stimulated Raman spectroscopy. *ACS Photonics* **6**, 492–500 (2019).
41. Tokmakoff, A. et al. Two-dimensional Raman spectroscopy of vibrational interactions in liquids. *Phys. Rev. Lett.* **79**, 2702 (1997).
42. Gillet, P., Le Cléac'h, A. & Madon, M. High-temperature Raman spectroscopy of SiO_2 and GeO_2 Polymorphs: Anharmonicity and thermodynamic properties at high-temperatures. *J. Geophys. Res.: Solid Earth* **95**, 21635–21655 (1990).
43. Castex, J. & Madon, M. Test of the vibrational modelling for the λ-type transitions: application to the α-β quartz transition. *Phys. Chem. Miner.* **22**, 1–10 (1995).
44. Ranieri, V. et al. Raman scattering study of α-quartz and Si 1− x Ge x O 2 solid solutions. *Phys. Rev. B* **79**, 224304 (2009).
45. Ouillon, R., Pinan-Lucarre, J. P. & Ranson, P. Anharmonicity of zone-centre optical phonons: Raman spectra of the isomorphous α-quartz, berlinite and gallium phosphate in the temperature range 8–300 K. *J. Raman Spectrosc.* **31**, 605–613 (2000).
46. Cho, M. et al. Intrinsic cascading contributions to the fifth- and seventh-order electronically off-resonant Raman spectroscopies. *J. Chem. Phys.* **112**, 2082–2094, https://doi.org/10.1063/1.480777 (2000).
47. Golonzka, O., Demirdöven, N., Khalil, M. & Tokmakoff, A. Separation of cascaded and direct fifth-order Raman signals using phase-sensitive intrinsic heterodyne detection. *J. Chem. Phys.* **113**, 9893–9896, https://doi.org/10.1063/1.1330236 (2000).
48. Pellegrini, C., Marinelli, A. & Reiche, S. The physics of x-ray free-electron lasers. *Rev. Mod. Phys.* **88**, 015006, https://doi.org/10.1103/RevModPhys.88.015006 (2016).
49. Duris, J. et al. Tunable isolated attosecond X-ray pulses with gigawatt peak power from a free-electron laser. *Nat. Photonics* **14**, 30–36, https://doi.org/10.1038/s41566-019-0549-5 (2020).
50. Kimberg, V. & Rohringer, N. Stochastic stimulated electronic x-ray Raman spectroscopy. *Struct. Dyn.* **3**, 034101, https://doi.org/10.1063/1.4940916 (2016).
51. Gorobtsov, O. Y. et al. Seeded X-ray free-electron laser generating radiation with laser statistical properties. *Nat. Commun.* **9**, 4498, https://doi.org/10.1038/s41467-018-06743-8 (2018).
52. Asban, S., Cho, D. & Mukamel, S. Frequency-, time-, and wavevector-resolved ultrafast incoherent diffraction of noisy X-ray pulses. *J. Phys. Chem. Lett.* **10**, 5805–5814, https://doi.org/10.1021/acs.jpclett.9b00924 (2019).
53. Kayser, Y. et al. Core-level nonlinear spectroscopy triggered by stochastic X-ray pulses. *Nat. Commun.* **10**, 4761, https://doi.org/10.1038/s41467-019-12717-1 (2019).
54. Driver, T. et al. Attosecond transient absorption spooktroscopy: a ghost imaging approach to ultrafast absorption spectroscopy. *Phys. Chem. Chem. Phys.* **22**, 2704–2712, https://doi.org/10.1039/c9cp03951a (2020).
55. Cavaletto, S. M., Keefer, D. & Mukamel, S. High temporal and spectral resolution of stimulated X-ray raman signals with stochastic free-electron-laser pulses. *Phys. Rev. X* **11**, 011029, https://doi.org/10.1103/physrevx.11.011029 (2021).
56. Cavaletto, S. M. et al. Unveiling the spatial distribution of molecular coherences at conical intersections by covariance X-ray diffraction signals. *Proc. Natl Acad. Sci. USA* **118**, e2105046118, https://doi.org/10.1073/pnas.2105046118 (2021).
57. Bennett, K., Zhang, Y., Kowalewski, M., Hua, W. & Mukamel, S. Multidimensional resonant nonlinear spectroscopy with coherent broadband x-ray pulses. *Phys. Scr.* **T169**, 014002, https://doi.org/10.1088/0031-8949/t169/1/014002 (2016).

Transient measurement of phononic states with covariance-based stochastic spectroscopy

Giorgia Sparapassi,[1,2] Stefano Cavaletto,[3] Jonathan Tollerud,[4,*] Angela Montanaro,[1,2] Filippo Glerean,[1,2] Alexandre Marciniak,[1,2] Francesca Giusti,[1,2] Shaul Mukamel,[3] and Daniele Fausti[1,2,†]

[1] *Physics Department, University of Trieste, 34127 Trieste, Italy*
[2] *Elettra-Sincrotrone Trieste S.C.p.A., 34149 Trieste, Italy*
[3] *Department of Chemistry and Department of Physics & Astronomy, University of California, Irvine, CA 92697, USA*
[4] *Optical Sciences Centre, Swinburne University, Melbourne, Australia, 3122*

(Dated: January 18, 2022)

S1. TIME- AND FREQUENCY-RESOLVED IMPULSIVE STIMULATED RAMAN SPECTROSCOPY SIGNAL

In this Supplementary Section, we derive the expressions for the impulsive stimulated Raman spectroscopy (ISRS) signal investigated in the main text. We derive expressions for a single phonon Ω and consider a manifold of vibrational states $|n\rangle$ of energy $\omega_n = \Omega(n+1/2)$. All expressions can be straightforwardly generalized by summing over all phonons.

In ISRS, two nonoverlapping pump and probe pulses, both off-resonant from electronic excited states, induce a sequence of impulsive stimulated Raman excitations, thereby coupling the vibrational states in the system. The effective interaction Hamiltonian in the rotating-wave approximation is given by [1]

$$\hat{H}_{\rm int}(t) = -\hat{\alpha}\left[|\mathcal{E}_1(t+T)|^2 + |\mathcal{E}_2(t)|^2\right], \tag{S1}$$

with the effective polarizability operator $\hat{\alpha}$ and classical electric fields

$$\mathcal{E}_i(t) = E_i(t)\,\mathrm{e}^{-\mathrm{i}\omega_{i0}t}, \tag{S2}$$

$i \in \{1, 2\}$, of envelopes $E_i(t)$, carrier frequencies ω_{i0}, and associated Fourier transforms

$$\tilde{\mathcal{E}}_i(\omega) = \int \mathrm{d}t\,\mathcal{E}_i(t)\,\mathrm{e}^{\mathrm{i}\omega t}, \qquad \mathcal{E}_i(t) = \frac{1}{2\pi}\int \mathrm{d}\omega\,\tilde{\mathcal{E}}_i(\omega)\,\mathrm{e}^{-\mathrm{i}\omega t}. \tag{S3}$$

The pump $\mathcal{E}_1(t+T)$ and probe $\mathcal{E}_2(t)$ pulses are centered around $t_{10} = -T$ and $t_{20} = 0$, respectively.

The ladder diagrams and level scheme of the ISRS signal are depicted in Fig. S1. For nonoverlapping pulses, the system is first excited by the pump pulse $\mathcal{E}_1(t+T)$ from an initial equilibrium state $\hat{\rho}^{(0)}$ to a coherent superposition of vibrational states. To first order in perturbation theory, the interaction with the pump pulse and the resulting evolution of the system's density matrix $\hat{\rho}(t)$, of elements $\rho_{nn'}(t)$, are given by

$$\rho_{nn'}(t) = \rho_{0,nn'} + \mathrm{i}\int_{-\infty}^{t} \mathrm{d}t'\,\mathrm{e}^{-\mathrm{i}\omega_{nn'}(t-t')}\,\mathrm{e}^{-\gamma(t-t')}\,\alpha_{nn'}\,|\mathcal{E}_1(t'+T)|^2\,\left(\rho^{(0)}_{n'n'} - \rho^{(0)}_{nn}\right), \tag{S4}$$

with the transition energies $\omega_{nn'} = \Omega(n-n')$ and decay rates γ. The two terms in the above sum, $\rho^{(0)}_{n'n'}$ and $\rho^{(0)}_{nn}$, are associated with the top and bottom diagrams in Fig. S1, respectively. For nonoverlapping pulses, we can extend the above integral to $t \to +\infty$, so that Eq. (S4) can be recast as

$$\rho_{nn'}(t) = \rho_{0,nn'} + \mathrm{i}\,\mathrm{e}^{-\mathrm{i}\omega_{nn'}(t+T)}\,\mathrm{e}^{-\gamma(t+T)}\int_{-\infty}^{+\infty} \mathrm{d}t'\,\mathrm{e}^{\mathrm{i}\omega_{nn'}t'}\,\mathrm{e}^{\gamma t'}\,\alpha_{nn'}\,|\mathcal{E}_1(t')|^2\,\left(\rho^{(0)}_{n'n'} - \rho^{(0)}_{nn}\right). \tag{S5}$$

The pump pulse used in the experiment is a coherent pulse of Gaussian envelope

$$\mathcal{E}_1(t) = E_{10}\,\mathrm{e}^{-\sigma_1^2 t^2/2}\,\mathrm{e}^{-\mathrm{i}\omega_{10}t}, \tag{S6}$$

* Email: jtollerud@swin.edu.au

† Email: daniele.fausti@elettra.eu

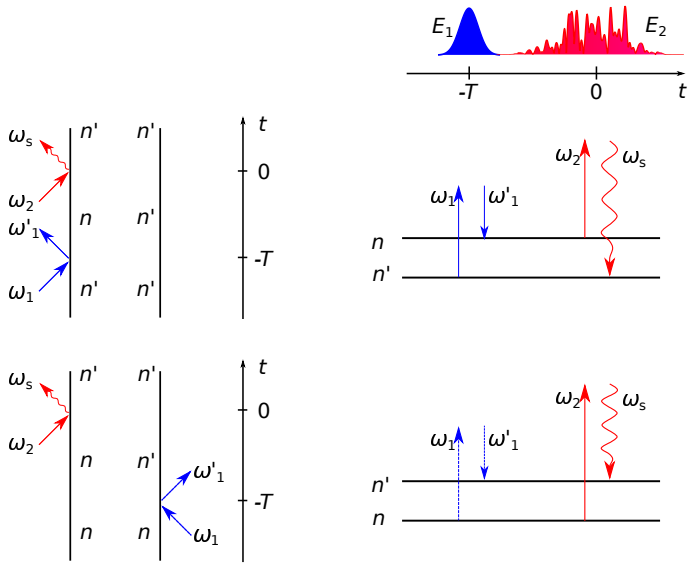

Figure S1. Ladder diagrams and level schemes for the third-order ISRS signal.

with central frequency $\omega_{10} = 230\,\mathrm{THz}$ (1300 nm), peak strength E_{10}, and bandwidth $\sigma_1 = 2.5\,\mathrm{THz}$ (110 fs duration). For such coherent Gaussian pulse, and for a system in the initial thermal state

$$\hat{\rho}^{(0)} = \sum_n \rho_{nn}^{(0)} \, |n\rangle\langle n| = \sum_n \frac{\mathrm{e}^{-\beta\Omega n}}{1-\mathrm{e}^{-\beta\Omega n}} \, |n\rangle\langle n|, \tag{S7}$$

with initial populations $\rho_{nn}^{(0)}$, $\beta = 1/(k_\mathrm{B}T_\mathrm{e})$, Boltzmann constant k_B, and temperature T_e, Eq. (S5) reduces to

$$\rho_{nn'}(t) = \rho_{nn}^{(0)} \, \delta_{nn'} + \rho_{nn'}^{(1)} \, \mathrm{e}^{-\mathrm{i}\Omega(n-n')(t+T)} \, \mathrm{e}^{-\gamma(t+T)} \tag{S8}$$

in terms of the first-order perturbation

$$\rho_{nn'}^{(1)} = \mathrm{i}\,|E_{10}|^2 \, \frac{\sqrt{\pi}}{\sigma_1} \, \mathrm{e}^{-\Omega^2(n-n')^2/(4\sigma_1^2)} \, \alpha_{nn'} \, \left(\rho_{n'n'}^{(0)} - \rho_{nn}^{(0)}\right). \tag{S9}$$

Due to the Gaussian envelope $\mathrm{e}^{-\Omega^2(n-n')^2/(4\sigma_1^2)}$ in Eq. (S9) and its finite bandwidth σ_1, we focus only on the matrix elements $\rho_{nn'}(t)$ for which either $n' = n$ or $n' = n \pm 1$, and neglect all remaining off-diagonal elements in Eq. (S8).

The evolution of the superposition of vibrational states generated by the pump pulse is monitored by a subsequent stimulated Raman process induced by the probe pulse $\mathcal{E}_2(t)$. The frequency-dispersed heterodyne-detected signal is defined as the time-integrated rate of change of photon number in the probe pulse [2]

$$S(\omega_\mathrm{s}, T) = -\int \mathrm{d}t \left\langle \frac{\mathrm{d}\hat{N}_{\omega_\mathrm{s}}^{(2)}(t)}{\mathrm{d}t} \right\rangle, \tag{S10}$$

where $\hat{N}_\omega = \hat{a}_\omega^\dagger \hat{a}_\omega$ denotes the number operator for a photon mode with frequency ω. The superscript "(2)" in $\hat{N}_{\omega_\mathrm{s}}^{(2)}$ stresses that the modes are restricted to those occupied by the probe pulse $\mathcal{E}_2(t)$. By using the Heisenberg equations of motion for the photon number operator, the signal at the detected frequency ω_s reads

$$S(\omega_\mathrm{s}) = 2\,\mathbf{Im}\left\{\tilde{\mathcal{E}}_2^*(\omega_\mathrm{s}) \int \mathrm{d}t\, \mathcal{E}_2(t) \mathrm{e}^{\mathrm{i}\omega_\mathrm{s}t} \langle\hat{\alpha}(t)\rangle\right\}, \tag{S11}$$

with the time-dependent polarizability

$$\langle\hat{\alpha}(t)\rangle = \mathrm{Tr}\{\hat{\alpha}\,\hat{\rho}(t)\} = \sum_{nn'} \alpha_{n'n}\,\rho_{nn'}(t). \tag{S12}$$

For nonoverlapping pulses, by expressing the elements of the density matrix via Eq. (S8), the time- and frequency-dependent ISRS signal can be recast as

$$\begin{aligned} S_{\mathrm{ISRS}}(\omega_\mathrm{s}, T) = {} & 2\,\mathbf{Im}\left\{\tilde{\mathcal{E}}_2^*(\omega_\mathrm{s})\,\tilde{\mathcal{E}}_2(\omega_\mathrm{s}-\Omega)\,A\,\mathrm{e}^{-\mathrm{i}\Omega T}\,\mathrm{e}^{-\gamma T}\right\} \\ & + 2\,\mathbf{Im}\left\{\tilde{\mathcal{E}}_2^*(\omega_\mathrm{s})\,\tilde{\mathcal{E}}_2(\omega_\mathrm{s}+\Omega)\,A^*\,\mathrm{e}^{\mathrm{i}\Omega T}\,\mathrm{e}^{-\gamma T}\right\}, \end{aligned} \tag{S13}$$

where

$$A = \sum_n \alpha_{n,n+1}\,\rho^{(1)}_{n+1,n} = \mathrm{i}\,|E_{10}|^2\,\frac{\sqrt{\pi}}{\sigma_1}\,\mathrm{e}^{-\Omega^2/(4\sigma_1^2)}\sum_n |\alpha_{n,n+1}|^2\,\left(\rho^{(0)}_{nn} - \rho^{(0)}_{n+1,n+1}\right) \tag{S14}$$

contains the amplitude and phase information of the vibrational coherence generated by the pump pulse. For $\alpha_{n,n+1} \approx \tilde{\alpha}$, this coherence term A reduces to

$$A \approx \mathrm{i}\,|E_{10}|^2\,\frac{\sqrt{\pi}}{\sigma_1}\,\mathrm{e}^{-\Omega^2/(4\sigma_1^2)}\,|\tilde{\alpha}|^2\,\frac{1}{1-\mathrm{e}^{-\beta\Omega}}. \tag{S15}$$

Additional features appear in the presence of overlapping pump and probe pulses, which are responsible for the hyperbola branches in the (ω_s, T) plane observed in the experiment. These features have been previously analyzed [3] and are not the focus of this work.

S2. MODELING OF THE STOCHASTIC PROBE PULSE

The stochastic probe pulse used in the experiment is obtained from an initial coherent pulse, here modeled as a Gaussian pulse

$$\tilde{g}_2(\omega) = \mathrm{e}^{-\omega^2/(2\sigma_2^2)} \tag{S16}$$

of bandwidth $\sigma_2 = 6.6\,\mathrm{THz}$ (40 fs duration). The pulse spectral phase $\varphi(\omega)$ is shaped by a pulse shaper with finite resolution $R = 0.1\,\mathrm{THz}$, leading to the shaped stochastic pulse

$$\tilde{\mathcal{E}}_{2,\mathrm{sh}}(\omega) = \tilde{E}_{20}\,\tilde{g}_2(\omega-\omega_{20})\,\mathrm{e}^{\mathrm{i}\varphi(\omega)}, \tag{S17}$$

with central frequency $\omega_{20} = 375\,\mathrm{THz}$ (800 nm) and peak strength E_{20}. In Sec. S5, a pulse with noise present only on part of its spectral width will be considered.

The spectral phase $\varphi(\omega)$ is obtained by generating an array of N independent random numbers φ_k for a discrete set of frequencies $\omega_k = \omega_{20} + kR$, $k \in \{-N/2,\, -N/2+1,\, \cdots,\, N/2-1\}$. Each number is randomly distributed in the interval $[-\bar{\varphi},\, \bar{\varphi}]$, with vanishing expectation value $\langle\varphi_k\rangle = 0$ and with $\langle\varphi_k\,\varphi_{k'}\rangle = \delta_{kk'}\,\bar{\varphi}^2/3$. This is convolved with a Gaussian smoothing function with width R, resulting in

$$\varphi(\omega) = \sum_k \varphi_k\,\mathrm{e}^{-(\omega-\omega_k)^2/(2R^2)}. \tag{S18}$$

The expectation value of the spectral phase is thus equal to

$$\langle\varphi(\omega)\rangle = 0 \tag{S19}$$

and its correlation function is given by

$$\langle\varphi(\omega)\varphi(\omega')\rangle = \langle\varphi^2\rangle\,\mathrm{e}^{-(\omega-\omega')^2/(4R^2)}, \tag{S20}$$

with the variance

$$\langle\varphi^2\rangle = \frac{\bar{\varphi}^2}{3}\sum_k \mathrm{e}^{-k^2}. \tag{S21}$$

In order to interpret the spectra obtained by the covariance approach used in the main text, we introduce the two- and four-point correlation functions of $\mathrm{e}^{\mathrm{i}\varphi(\omega)}$, defined as

$$\tilde{F}_2(\omega_1,\omega_2) \doteq \langle\mathrm{e}^{-\mathrm{i}\varphi(\omega_1)}\,\mathrm{e}^{\mathrm{i}\varphi(\omega_2)}\rangle \tag{S22}$$

and

$$\tilde{F}_4(\omega_1,\omega_2,\omega_3,\omega_4) \doteq \langle \mathrm{e}^{-\mathrm{i}\varphi(\omega_1)}\,\mathrm{e}^{\mathrm{i}\varphi(\omega_2)}\,\mathrm{e}^{-\mathrm{i}\varphi(\omega_3)}\,\mathrm{e}^{\mathrm{i}\varphi(\omega_4)}\rangle, \tag{S23}$$

respectively. To calculate these field correlation functions, we first introduce the correlation function $\langle\dot{\varphi}(\omega)\dot{\varphi}(\omega')\rangle$ of the first derivative of the spectral phase $\dot{\varphi}(\omega) = \mathrm{d}\varphi/\,\mathrm{d}\omega$. The stochastic probe pulse employed here is a wide-sense stationary process, for which

$$\langle\dot{\varphi}(\omega)\dot{\varphi}(\omega')\rangle = \tilde{q}(\omega-\omega') = \frac{\langle\varphi^2\rangle}{2R^2}\,\mathrm{e}^{-(\omega-\omega')^2/(4R^2)}\left(1-\frac{(\omega-\omega')^2}{2R^2}\right) \tag{S24}$$

only depends on the difference $\omega-\omega'$. We thus introduce the function

$$\tilde{p}(\omega) \doteq \int_0^\omega \mathrm{d}x\int_0^\omega \mathrm{d}y\,\langle\dot{\varphi}(x)\dot{\varphi}(y)\rangle = 2\,\langle\varphi^2\rangle\,\left(1-\mathrm{e}^{-\omega^2/(4R^2)}\right) \tag{S25}$$

and use the second-order cumulant expansion to write the two- [Eq. (S22)] and four-point [Eq. (S23)] correlation functions in terms of $\tilde{p}(\omega)$ [4], leading to the following identities:

$$\tilde{F}_2(\omega_1,\omega_2) = \mathrm{e}^{-\tilde{p}(\omega_1-\omega_2)/2} \tag{S26}$$

and

$$\tilde{F}_4(\omega_1,\omega_2,\omega_3,\omega_4) = \mathrm{e}^{-[\tilde{p}(\omega_1-\omega_2)-\tilde{p}(\omega_1-\omega_3)+\tilde{p}(\omega_1-\omega_4)+\tilde{p}(\omega_2-\omega_3)-\tilde{p}(\omega_2-\omega_4)+\tilde{p}(\omega_3-\omega_4)]/2}. \tag{S27}$$

We notice that $\tilde{F}_2(\omega_1,\omega_2) = \tilde{F}_2(\omega_1-\tilde{\omega},\omega_2-\tilde{\omega})$ and $\tilde{F}_4(\omega_1,\omega_2,\omega_3,\omega_4) = \tilde{F}_4(\omega_1-\tilde{\omega},\omega_2-\tilde{\omega},\omega_3-\tilde{\omega},\omega_4-\tilde{\omega})$ for any $\tilde{\omega}$.

The two-point correlation function $F_{2,\mathrm{sh}}(\omega,\omega')$ of the spectral pulse $\tilde{\mathcal{E}}_{2,\mathrm{sh}}(\omega)$ can be calculated in terms of $\tilde{F}_2(\omega,\omega')$ and is equal to

$$\begin{aligned} F_{2,\mathrm{sh}}(\omega,\omega') &\doteq \langle\tilde{\mathcal{E}}^*_{2,\mathrm{sh}}(\omega)\tilde{\mathcal{E}}_{2,\mathrm{sh}}(\omega')\rangle = |\tilde{E}_{20}|^2\,\tilde{g}_2(\omega-\omega_{20})\,\tilde{g}_2(\omega'-\omega_{20})\,\tilde{F}_2(\omega,\omega') \\ &= |\tilde{E}_{20}|^2\,\tilde{g}_2(\omega-\omega_{20})\,\tilde{g}_2(\omega'-\omega_{20})\,\exp\left(-\langle\varphi^2\rangle\,\left(1-\mathrm{e}^{-(\omega-\omega')^2/(4R^2)}\right)\right). \end{aligned} \tag{S28}$$

Figures S2 and S3 show the frequency and time properties of a numerical simulation of the stochastic pulses in Eq. (S17), for values of the variance $\langle\varphi^2\rangle = (\pi/4)^2$ and $\langle\varphi^2\rangle = (\pi/2)^2$, respectively. We notice in particular that, due to the method used to generate the stochastic spectral phases, these do not uniformly cover the whole phase interval $[-\pi,\,\pi]$. This is evident when $\langle\varphi^2\rangle = (\pi/4)^2$, and is still the case even for $\langle\varphi^2\rangle = (\pi/2)^2$. As a result, the amplitude of the average stochastic pulse $\langle\tilde{\mathcal{E}}_{2,\mathrm{sh}}(\omega)\rangle$ does not vanish, even though its peak value reduces for increasing values of $\langle\varphi^2\rangle$. In time domain, this results in the appearance of a central peak surrounded by a noisy tail: this central peak survives in the envelope of the average stochastic pulse $\langle E_{2,\mathrm{sh}}(t)\rangle$, whereas the noisy tails average out to 0.

The two panels in Fig. S4 show the associated correlation functions $\langle\dot{\varphi}(\omega)\dot{\varphi}(\omega')\rangle$ [Eq. (S24)] and $\langle\tilde{\mathcal{E}}^*_{2,\mathrm{sh}}(\omega)\tilde{\mathcal{E}}_{2,\mathrm{sh}}(\omega')\rangle$ [Eq. (S28)]. The curves display the behaviour of the correlation functions for $\langle\varphi^2\rangle = (\pi/4)^2$ and $\langle\varphi^2\rangle = (\pi/2)^2$. The correlation function of the first derivative of the spectral phase shows an oscillatory behavior, with a strong positive central peak surrounded by two negative peaks. For very close frequencies ω and ω' lying within the width of the central peak, the associated spectral phases will have correlated first derivatives $\dot{\varphi}(\omega)$ and $\dot{\varphi}(\omega')$ with the same sign. However, for increasing frequency differences, the spectral phases do not become directly uncorrelated: when the frequencies ω and ω' lie within the width of the second negative peak, this means that the associated spectral phases are still correlated, with first derivatives $\dot{\varphi}(\omega)$ and $\dot{\varphi}(\omega')$ exhibiting opposite sign. As a result, the autocorrelation of the field $\langle\tilde{\mathcal{E}}^*_{2,\mathrm{sh}}(\omega)\tilde{\mathcal{E}}_{2,\mathrm{sh}}(\omega')\rangle$ features one strong central peak. Out of this peak, however, the stochastic pulse still presents a nonvanishing autocorrelation function. The amplitude of this residual autocorrelation decreases with increasing values of the variance $\langle\varphi^2\rangle$.

In the experiment, the stochastic probe pulse was obtained by shaping its spectral phase. Nevertheless, the measured spectral intensity $|\tilde{\mathcal{E}}_2(\omega)|^2$ features chaotic oscillations as apparent in Fig. 1b in the main text. This is due to the finite resolution Q of the optical detector. The detected field is given by the convolution of the stochastic probe pulse $\tilde{\mathcal{E}}_{2,\mathrm{sh}}(\omega)$ generated by the pulse shaper and the function $q_Q(\omega)$ modeling the finite resolution of the optical detector

$$\tilde{\mathcal{E}}_2(\omega) = \int \mathrm{d}\omega'\,\tilde{\mathcal{E}}_{2,\mathrm{sh}}(\omega-\omega')\,q_Q(\omega'). \tag{S29}$$

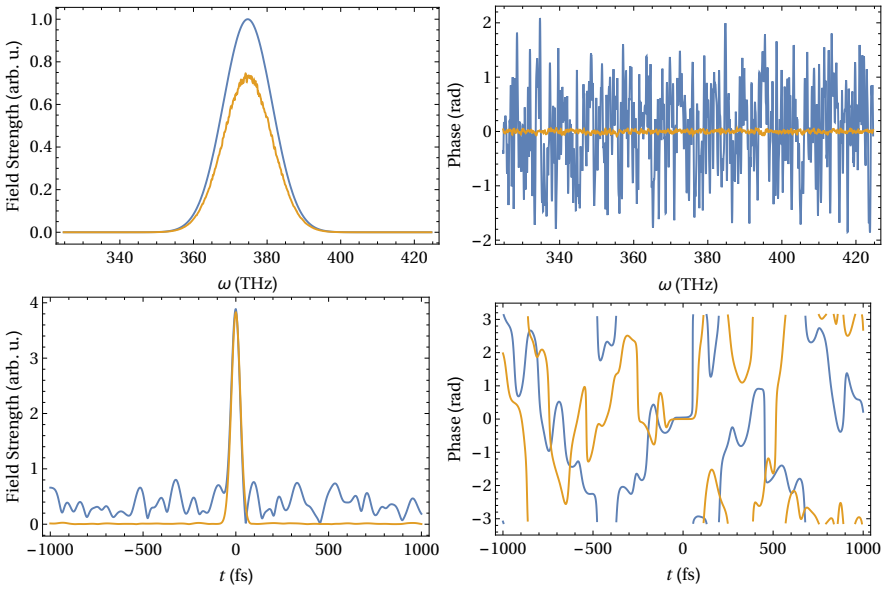

Figure S2. Numerical simulation of the stochastic probe pulses in Eq. (S17) for $\langle\varphi^2\rangle = (\pi/4)^2$. The first row shows the spectral properties of the pulse, by exhibiting (left) the amplitude and (right) the phase of (blue) one realization of the stochastic probe pulse $\tilde{\mathcal{E}}_{2,\mathrm{sh}}(\omega)$ and (yellow) an average over 1,000 independent realizations. The second row shows the temporal properties of the same stochastic pulses, i.e., (left) the amplitude and (right) the phase of (blue) one realization of the envelope $E_{2,\mathrm{sh}}(t)$ of the stochastic probe pulse and (yellow) an average over 1,000 independent realizations.

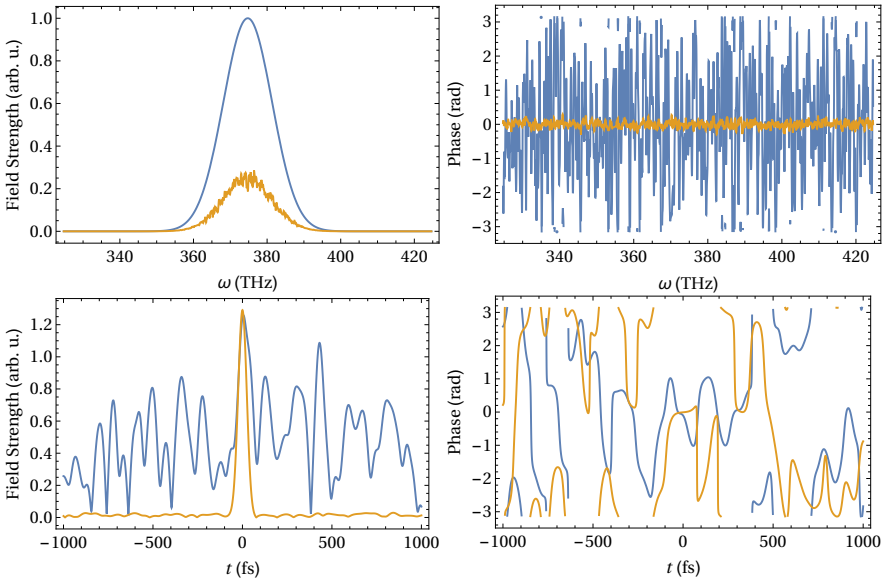

Figure S3. Numerical simulation of the stochastic probe pulses in Eq. (S17) for $\langle\varphi^2\rangle = (\pi/2)^2$. The different panels show the same properties of the pulses as in Fig. S2.

The spectral gating function $q_Q(\omega)$ acts over the fast random oscillations of $\mathrm{e}^{\mathrm{i}\varphi}$, affecting both amplitude and phase of $\tilde{\mathcal{E}}_2(\omega)$ and leading the the intensity fluctuations depicted in Fig. 1b in the main text. The two- and four-point correlation functions of the detected field are thus given by

$$\begin{aligned} &F_2(\omega_1,\omega_2) \doteq \langle \tilde{\mathcal{E}}_2^*(\omega_1)\tilde{\mathcal{E}}_2(\omega_2)\rangle \\ &= |\tilde{E}_{20}|^2\, \tilde{g}_2(\omega_1-\omega_{20})\, \tilde{g}_2(\omega_2-\omega_{20}) \int \mathrm{d}\omega_1' \int \mathrm{d}\omega_2'\, \tilde{F}_2(\omega_1-\omega_1',\omega_2-\omega_2')\, q_Q(\omega_1')\, q_Q(\omega_2') \end{aligned} \tag{S30}$$

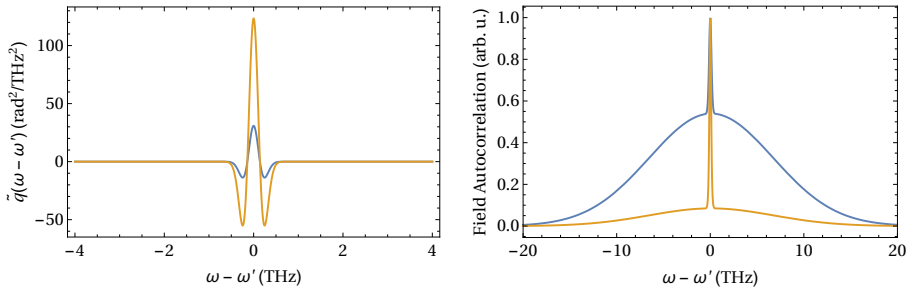

Figure S4. Correlation functions (left) $\tilde{q}(\omega-\omega')=\langle\dot{\varphi}(\omega)\dot{\varphi}(\omega')\rangle$ [Eq. (S24)] and (right) $F_{2,\mathrm{sh}}(\omega,\omega')=\langle\tilde{\mathcal{E}}^*_{2,\mathrm{sh}}(\omega)\tilde{\mathcal{E}}_{2,\mathrm{sh}}(\omega')\rangle$ [Eq. (S28)] of the stochastic probe pulses in Eq. (S17) for (blue) $\langle\varphi^2\rangle=(\pi/4)^2$ and (yellow) $\langle\varphi^2\rangle=(\pi/2)^2$.

and

$$\begin{aligned}
&F_4(\omega_1,\omega_2,\omega_3,\omega_4)\doteq\langle\tilde{\mathcal{E}}^*_2(\omega_1)\tilde{\mathcal{E}}_2(\omega_2)\tilde{\mathcal{E}}^*_2(\omega_3)\tilde{\mathcal{E}}_2(\omega_4)\rangle\\
&=|\tilde{E}_{20}|^4\,\tilde{g}_2(\omega_1-\omega_{20})\,\tilde{g}_2(\omega_2-\omega_{20})\,\tilde{g}_2(\omega_3-\omega_{20})\,\tilde{g}_2(\omega_4-\omega_{20})\\
&\quad\times\int\mathrm{d}\omega_1'\int\mathrm{d}\omega_2'\int\mathrm{d}\omega_3'\int\mathrm{d}\omega_4'\,\tilde{F}_4(\omega_1-\omega_1',\omega_2-\omega_2',\omega_3-\omega_3',\omega_4-\omega_4')\,q_Q(\omega_1')\,q_Q(\omega_2')\,q_Q(\omega_3')\,q_Q(\omega_4'),
\end{aligned}\tag{S31}$$

where we moved the broadband Gaussian envelopes $\tilde{g}(\omega)$ out of the integrals. In the following, we will model

$$q_Q(\omega)=\frac{1}{Q}\,\mathrm{rect}\left(\frac{\omega}{Q}\right)\tag{S32}$$

as a rectangular function of width $Q=0.1\,\mathrm{THz}$ and unit area, and we will use Eqs. (S26) and (S27) to perform the integrals in Eqs. (S30) and (S31) numerically.

Equation (S29) has a similar structure as models recently employed to describe the stochastic features of hard-x-ray free-electron-laser pulses generated by the self-amplified spontaneous emission methods [4–7]. In these x-ray models, a spectral gating function is included in order to reproduce the finite pulse duration and the corresponding coherence width of the spikes in the frequency envelope of the pulse. This is achieved by setting a spectral correlation length (the equivalent of Q) much larger than the correlation length of the pure phase fluctuations (the equivalent of R). This differs from this work, where the spectral gating function is included to reproduce the finite resolution of the optical detector, and where we set $Q=R$. This determines the shape of the two- and four-point field correlation functions, which will be discussed in the following.

S3. COVARIANCE-BASED SPECTROSCOPY AND PEARSON COEFFICIENTS

In this Supplementary Section, we define the Pearson coefficients analyzed in the main text. The experiment is repeated for independent realizations of a stochastic probe, and the spectra are quantified via the Pearson coefficient

$$P(I_1(\omega_{\mathrm{s}1}),I_2(\omega_{\mathrm{s}2}))=\frac{\langle I_1(\omega_{\mathrm{s}1})I_2(\omega_{\mathrm{s}2})\rangle-\langle I_1(\omega_{\mathrm{s}1})\rangle\langle I_2(\omega_{\mathrm{s}2})\rangle}{\sigma_1(\omega_{\mathrm{s}1})\sigma_2(\omega_{\mathrm{s}2})},\tag{S33}$$

where $I_1(\omega_{\mathrm{s}1})$ and $I_2(\omega_{\mathrm{s}2})$ can either be the detected input intensity of the probe pulse [$\tilde{\mathcal{E}}_2(\omega_{\mathrm{s}})$ in Eq. (S29)] before interaction with the sample

$$I_{\mathrm{in}}(\omega_{\mathrm{s}})=\tilde{\mathcal{E}}^*_2(\omega_{\mathrm{s}})\tilde{\mathcal{E}}_2(\omega_{\mathrm{s}}),\tag{S34}$$

or the detected output intensity of the probe pulse after transmitting through the sample

$$I_{\mathrm{out}}(\omega_{\mathrm{s}},T)=I_{\mathrm{in}}(\omega_{\mathrm{s}})+S(\omega_{\mathrm{s}},T).\tag{S35}$$

In the definition of the Pearson coefficient, $\sigma_i(\omega_{\mathrm{s}i})$ denotes the standard deviation of $I_i(\omega_i)$ given by

$$\sigma_i(\omega_{\mathrm{s}i})=\sqrt{\langle I_i^2(\omega_{\mathrm{s}i})\rangle-\langle I_i(\omega_{\mathrm{s}i})\rangle^2}.\tag{S36}$$

In the following, we will focus on the autocorrelation of the input intensity,

$$P(I_{\rm in}(\omega_{\rm s1}), I_{\rm in}(\omega_{\rm s2})) = \frac{\langle I_{\rm in}(\omega_{\rm s1}) I_{\rm in}(\omega_{\rm s2})\rangle - \langle I_{\rm in}(\omega_{\rm s1})\rangle\langle I_{\rm in}(\omega_{\rm s2})\rangle}{\sigma_{\rm in}(\omega_{\rm s1})\sigma_{\rm in}(\omega_{\rm s2})}, \tag{S37}$$

and the cross-correlation

$$\begin{aligned} P(I_{\rm in}(\omega_{\rm s1}, T), I_{\rm out}(\omega_{\rm s2}, T)) = &\frac{\langle I_{\rm in}(\omega_{\rm s1}) I_{\rm in}(\omega_{\rm s2})\rangle - \langle I_{\rm in}(\omega_{\rm s1})\rangle\langle I_{\rm in}(\omega_{\rm s2})\rangle}{\sigma_{\rm in}(\omega_{\rm s1})\sigma_{\rm out}(\omega_{\rm s2}, T)} \\ &+ \frac{\langle I_{\rm in}(\omega_{\rm s1}) S(\omega_{\rm s2}, T)\rangle - \langle I_{\rm in}(\omega_{\rm s1})\rangle\langle S(\omega_{\rm s2}, T)\rangle}{\sigma_{\rm in}(\omega_{\rm s1})\sigma_{\rm out}(\omega_{\rm s2}, T)} \end{aligned} \tag{S38}$$

of input and output intensities. In all above formulas, the signal–signal correlation terms have not been included since they are weaker than the correlation between input intensity and signal.

The cross-correlation $P(I_{\rm in}(\omega_{\rm s1}, T), I_{\rm out}(\omega_{\rm s2}, T))$ corresponds to three-dimensional matrix $\rho_{\rm c}(\omega_{\rm IN}, \omega_{\rm OUT}, T)$ displayed in Fig. 1c in the main text, where $\omega_{\rm s1} = \omega_{\rm IN}$ and $\omega_{\rm s2} = \omega_{\rm OUT}$. As shown in Eq. (S38), this cross-correlation contains two main contributions, owing to the autocorrelation of the input pulse and the cross-correlation between input intensity and ISRS signal, respectively. This latter term,

$$P_{I,S}(\omega_{\rm s1}, \omega_{\rm s2}, T) = \frac{\langle I_{\rm in}(\omega_{\rm s1}) S_{\rm ISRS}(\omega_{\rm s2}, T)\rangle - \langle I_{\rm in}(\omega_{\rm s1})\rangle\langle S_{\rm ISRS}(\omega_{\rm s2}, T)\rangle}{\sigma_{\rm in}(\omega_{\rm s1})\,\sigma_{\rm out}(\omega_{\rm s2})}, \tag{S39}$$

is responsible for the off-diagonal lines appearing in the bottom-right quadrant of the correlation map displayed in Fig. 1c in the main text, and is therefore the term we will focus on in the following.

S4. AUTO- AND CROSS-CORRELATIONS FOR A STOCHASTIC PROBE WITH NOISE DISTRIBUTED IN THE ENTIRE SPECTRAL BANDWIDTH

In the main text, we presented results for the partially stochastic pulses of Fig. 1b, where the pulse is shaped only at frequencies larger than 370 THz. For modeling purposes, we here start by describing the case of a pulse with noise distributed in its entire spectral bandwidth. The case of a partially shaped pulse is presented in Sec. S5.

In this Supplementary Section, we therefore consider the stochastic probe pulse of Eq. (S17), with noise distributed on the whole frequency spectrum. We set $\langle\varphi^2\rangle = (\pi/2)^2$ and include the effect of the finite resolution of the optical detector via Eq. (S29) as a rectangular function $q_Q(\omega)$ [Eq. (S32)] of width $Q = 0.1$ THz. Different choices of the function modeling the optical detector do not modify our conclusions. We consider nonoverlapping pump and probe pulses, so that the signal $S(\omega_{\rm s}, T)$ contributing to the output intensity $I_{\rm out}(\omega_{\rm s}, T)$ is given by $S_{\rm ISRS}(\omega_{\rm s}, T)$ in Eq. (S13). The Pearson coefficients for auto- and cross-correlation of input and output intensities are exemplified for a system with a single phonon of frequency $\Omega = 10$ THz and lifetime $1/\gamma = 1.6$ ps.

A simulation of the autocorrelation of the detected input intensity, given by the Pearson coefficient $P(I_{\rm in}(\omega_{\rm s1}), I_{\rm in}(\omega_{\rm s2}))$ in Eq. (S37), is shown in Fig. S5. This is calculated in terms of the two- [Eq. (S30)] and

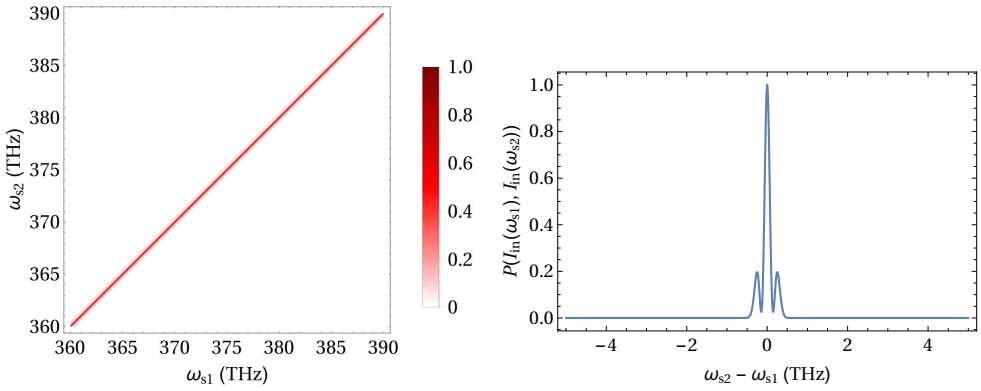

Figure S5. Pearson coefficient $P(I_{\rm in}(\omega_{\rm s1}), I_{\rm in}(\omega_{\rm s2}))$ of the autocorrelation of the detected input intensity for a fully modulated stochastic probe pulse (left) as a function of the two frequencies $\omega_{\rm s1}$ and $\omega_{\rm s2}$ and (right) as a function of the frequency difference $\omega_{\rm s1} - \omega_{\rm s2}$ for $(\omega_{\rm s1} + \omega_{\rm s2})/2 = 374$ THz.

four-point [Eq. (S31)] correlation functions of the detected field as

$$P(I_{\rm in}(\omega_{\rm s1}), I_{\rm in}(\omega_{\rm s2})) = \frac{F_4(\omega_{\rm s1},\omega_{\rm s1},\omega_{\rm s2},\omega_{\rm s2}) - F_2(\omega_{\rm s1},\omega_{\rm s1})\,F_2(\omega_{\rm s2},\omega_{\rm s2})}{\sigma_{\rm in}(\omega_{\rm s1})\,\sigma_{\rm in}(\omega_{\rm s2})}, \tag{S40}$$

with the standard deviation

$$\sigma_{\rm in}(\omega_{si}) = \sqrt{F_4(\omega_{si},\omega_{si},\omega_{si},\omega_{si}) - [F_2(\omega_{si},\omega_{si})]^2}. \tag{S41}$$

Figure S5 exhibits a strong peak along the main diagonal $\omega_{\rm s1} = \omega_{\rm s2}$ with width determined by the pulse-shaper and optical-detector resolutions. We notice also the presence of additional, lower-intensity peaks around the central one, as visible on the right panel of Fig. S5.

When input and output intensity are cross-correlated, the resulting signal carries the additional contribution due to $P_{I,S}(\omega_{\rm s1},\omega_{\rm s2},T)$ from Eq. (S39). With the expression for the signal in Eq. (S13), this contribution reads

$$P_{I,S}(\omega_{\rm s1},\omega_{\rm s2},T) = \frac{2\,\mathbf{Im}\left\{G(\omega_{\rm s1},\omega_{\rm s2},\Omega)\,A\,{\rm e}^{-{\rm i}\Omega T}\,{\rm e}^{-\gamma T} + G(\omega_{\rm s1},\omega_{\rm s2},-\Omega)\,A^*\,{\rm e}^{{\rm i}\Omega T}\,{\rm e}^{-\gamma T}\right\}}{\sigma_{\rm in}(\omega_{\rm s1})\,\sigma_{\rm out}(\omega_{\rm s2})}, \tag{S42}$$

where we have defined the functions

$$\begin{aligned} G(\omega_{\rm s1},\omega_{\rm s2},\pm\Omega) &\doteq F_4(\omega_{\rm s1},\omega_{\rm s1},\omega_{\rm s2},\omega_{\rm s2}\mp\Omega) - F_2(\omega_{\rm s1},\omega_{\rm s1})\,F_2(\omega_{\rm s2},\omega_{\rm s2}\mp\Omega) \\ &= |\tilde{E}_{20}|^4\,\tilde{g}_2^2(\omega_{\rm s1}-\omega_{20})\,\tilde{g}_2(\omega_{\rm s2}-\omega_{20})\,\tilde{g}_2(\omega_{\rm s2}\mp\Omega-\omega_{20})\,\tilde{G}(\omega_{\rm s2}-\omega_{\rm s1},\pm\Omega) \end{aligned} \tag{S43}$$

and

$$\begin{aligned} \tilde{G}(\omega_{\rm R},\pm\Omega) \doteq \int {\rm d}x \int {\rm d}x' \int {\rm d}y \int {\rm d}y'\, q_Q(x)\,q_Q(x')\,q_Q(y)\,q_Q(y') \\ \times [\tilde{F}_4(-x,-x',\omega_{\rm R}-y,\omega_{\rm R}\mp\Omega-y') - \tilde{F}_2(-x,-x')\,\tilde{F}_2(-y,\mp\Omega-y')]. \end{aligned} \tag{S44}$$

The correlation function $P_{I,S}(\omega_{\rm s1},\omega_{\rm s2},T)$ depends separately on $\omega_{\rm s1}$ and $\omega_{\rm s2}$ due to the presence of the Gaussian envelopes $\tilde{g}_2(\omega-\omega_{20})$. However, for sufficiently broadband pulses, the key features of $P_{I,S}(\omega_{\rm s1},\omega_{\rm s2},T)$ are determined by $\tilde{G}(\omega_{\rm s2}-\omega_{\rm s1},\pm\Omega)$, which depends on $\omega_{\rm s1}$ and $\omega_{\rm s2}$ only via the Raman frequency

$$\omega_{\rm R} \doteq \omega_{\rm s2} - \omega_{\rm s1}. \tag{S45}$$

This is the equivalent of $\delta\omega$ in the main text. The function $\tilde{G}(\omega_{\rm R},\pm\Omega)$ is responsible for the off-diagonal features observed in the experimental spectra of Fig. 1c in the main text. We calculate it numerically, including the effect of the finite resolution of the optical detector, and display it in the left panel of Fig. S6. The function exhibits a structure consisting of two main peaks,

$$\tilde{G}(\omega_{\rm R},\pm\Omega) = \tilde{f}(\omega_{\rm R}) + \tilde{f}(\omega_{\rm R}\mp\Omega), \tag{S46}$$

centered on $\omega_{\rm R} = 0$ and $\omega_{\rm R} = \pm\Omega$, respectively. The shape of each peak, $\tilde{f}(\omega_{\rm R})$, is highlighted in the right panel of Fig. S6. It contains two narrow peaks, mostly determined by the correlation length R of the stochastic pulses used. We could check numerically that the function $q_Q(\omega)$, modeling the optical detector, influences the width of the two peaks and the depth of the central local minimum appearing in $\tilde{f}(\omega)$. However, this does not affect the central frequency of the peaks in $\tilde{G}(\omega_{\rm R},\pm\Omega)$. Scanning the Raman frequency $\omega_{\rm R}$ allows one to identify the energy $\pm\Omega$ of the phonons in the system.

The resulting function $P_{I,S}(\omega_{\rm s1},\omega_{\rm s2},T)$ is displayed in Fig. S7. Two peaks along $\omega_{\rm s2}-\omega_{\rm s1} = \pm\Omega$ are clearly visible in the left panel, due to $\tilde{f}(\omega_{\rm R}\mp\Omega)$ in $\tilde{G}(\omega_{\rm R},\pm\Omega)$. In the right panel, we highlight the oscillations displayed by both peaks as a function of time delay. The oscillations along the two peaks take place at a frequency given by Ω and have opposite phase, owing to the π shift between the initial coherences, A and A^*, generated by the pump pulse. The envelope $\tilde{g}(\omega_{\rm s}-\omega_{20})$ of the probe pulse determines the dependence of the standard deviations $\sigma_i(\omega_{\rm s})$ upon frequency. $\tilde{g}(\omega_{\rm s}-\omega_{20})$ and, thus, $\sigma_i(\omega_{\rm s})$ become very small far from the central frequency ω_{20}. The corresponding increase in the strength of the peaks is apparent in the left panel of Fig. S7.

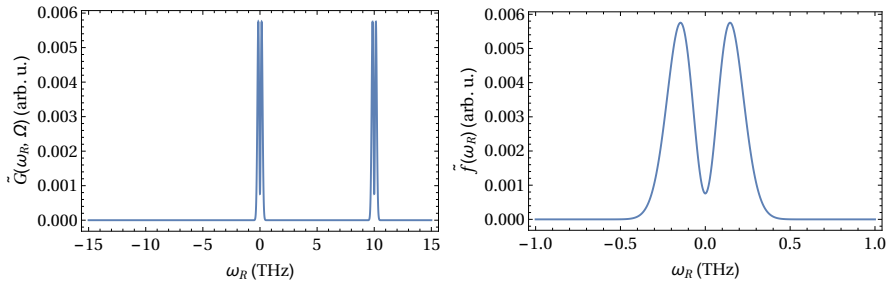

Figure S6. (left) $\tilde{G}(\omega_{\mathrm{R}}, \Omega)$ between the spectral function of the detected probe pulse evaluated at four different frequencies. (right) Peak $\tilde{f}(\omega_{\mathrm{R}})$ appearing $\tilde{G}(\omega_{\mathrm{R}}, \Omega)$.

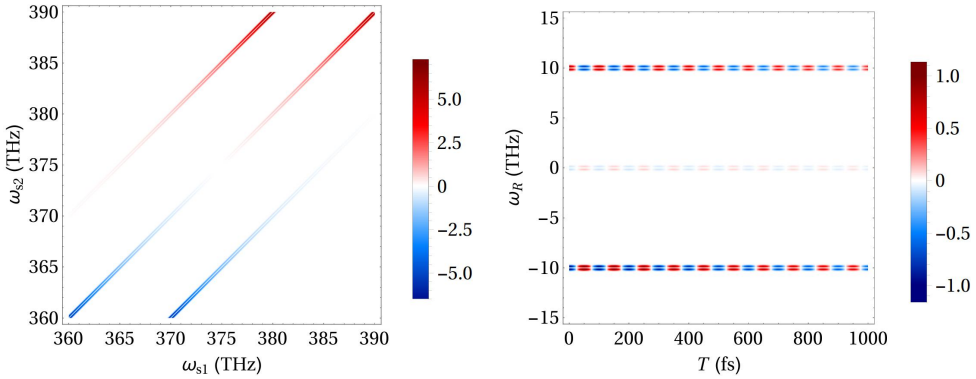

Figure S7. $P_{I,S}(\omega_{\mathrm{s1}}, \omega_{\mathrm{s2}}, T))$ for a fully modulated stochastic probe pulse. The cross-correlation function is displayed (left) as a function of the two frequencies ω_{s1} and ω_{s2} for $T = 500\,\mathrm{fs}$, and (right) as a function of the Raman frequency ω_{R} and time delay T for a mean frequency $(\omega_{\mathrm{s1}} + \omega_{\mathrm{s2}})/2 = 374\,\mathrm{THz}$.

S5. AUTO- AND CROSS-CORRELATIONS FOR A STOCHASTIC PROBE WITH NOISE PARTIALLY DISTRIBUTED IN THE SPECTRAL BANDWIDTH

In this Supplementary Section, we consider a stochastic probe pulse with noise only partially distributed within the spectral width of the pulse, i.e.,

$$\tilde{\mathcal{E}}_{2,\mathrm{sh}}(\omega) = \tilde{E}_{20}\, \tilde{g}_2(\omega - \omega_{20}) \left[\theta(-(\omega - \omega_{\mathrm{th}})) + \theta(\omega - \omega_{\mathrm{th}})\, \mathrm{e}^{\mathrm{i}\varphi(\omega)}\right], \tag{S47}$$

where we have introduced the Heaviside step function $\theta(x)$ and the threshold frequency $\omega_{\mathrm{th}} = 370\,\mathrm{THz}$, below which no spectral shaping is introduced. This corresponds to the experimental pulse of Fig. 1b in the main text. We assume $\langle\varphi^2\rangle = (\pi/2)^2$ and model the finite resolution of the optical detector via the rectangular function in Eq. (S32), with $Q = 0.1\,\mathrm{THz}$. We consider nonoverlapping pump and probe pulses, with the signal given by the ISRS spectrum $S_{\mathrm{ISRS}}(\omega_{\mathrm{s}}, T)$ of Eq. (S13), and study the dynamics of one single phonon of frequency $\Omega = 10\,\mathrm{THz}$ and lifetime $1/\gamma = 1.6\,\mathrm{ps}$. For ω_{s1} and ω_{s2} both greater than the threshold frequency, the same auto- and cross-correlations are expected as in Sec. S4. However, when at least one of these two frequencies is lower than ω_{th}, a different behavior is observed. This is discussed in the following for the input-intensity autocorrelation and for the cross-correlation between input pulse and signal.

Figure S8 exhibits the autocorrelation function of the detected input intensity [Eq. (S37)]. For $\omega_{\mathrm{s1}} > \omega_{\mathrm{th}}$ and $\omega_{\mathrm{s2}} > \omega_{\mathrm{th}}$, the same peak along the main diagonal $\omega_{\mathrm{s1}} = \omega_{\mathrm{s2}}$ is found as in Fig. S5. For frequencies lower then ω_{th}, however, where the spectral phase is unshaped, the associated standard deviation $\sigma_{\mathrm{in}}(\omega_{\mathrm{s}})$ would vanish exactly in our model, and the associated Pearson coefficient $P(I_{\mathrm{in}}(\omega_{\mathrm{s1}}), I_{\mathrm{in}}(\omega_{\mathrm{s2}}))$ in Eq. (S37) would diverge. To avoid this divergence and obtain simulation results in agreement with the experiment, we assume here and in the following a small, finite standard deviation ϵ at frequencies $\omega < \omega_{\mathrm{th}}$ where the pulse does not undergo any modulation of the spectral phase. This simple assumption allows us to obtain results in agreement with the experimental analysis.

Figure S9 displays the cross-correlation $P_{I,S}(\omega_{\mathrm{s1}}, \omega_{\mathrm{s2}}, T)$ between the input intensity of the probe pulse and the ISRS signal. In order to understand the behavior of the cross-correlation function, we first observe that for $\omega_{\mathrm{s1}} < \omega_{\mathrm{th}}$, where the input intensity does not feature any added noise, no correlation can exist between $I_{\mathrm{in}}(\omega_{\mathrm{s1}})$ and the signal

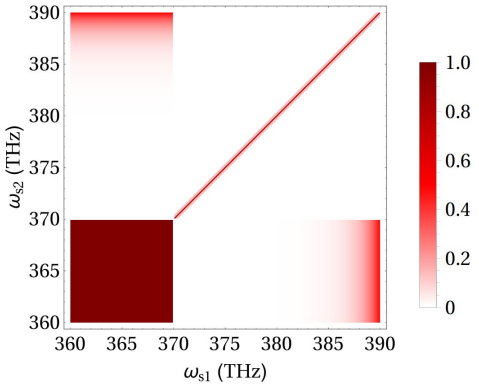

Figure S8. Pearson coefficient $P(I_{\mathrm{in}}(\omega_{\mathrm{s1}}), I_{\mathrm{in}}(\omega_{\mathrm{s2}}))$ of the autocorrelation of the detected input intensity for a partially modulated stochastic probe pulse.

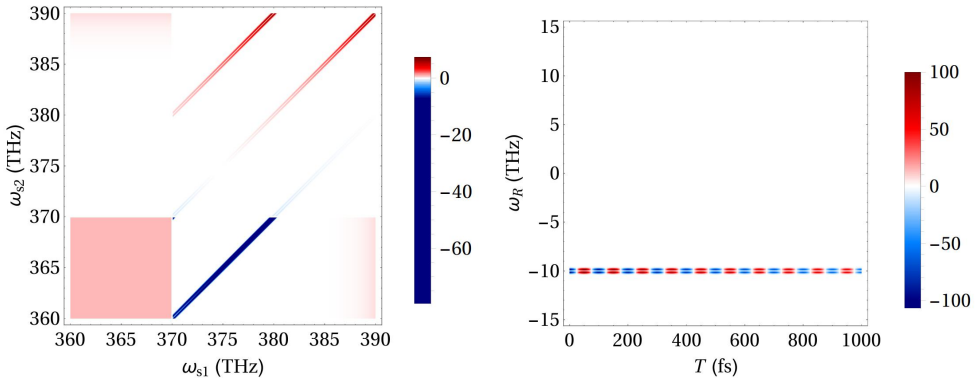

Figure S9. Contribution of the correlation function between the detected input intensity of the probe pulse and the ISRS signal to the Pearson coefficient $P(I_{\mathrm{in}}(\omega_{\mathrm{s1}}), I_{\mathrm{out}}(\omega_{\mathrm{s2}}, T))$ for a partially modulated stochastic probe pulse. The cross-correlation function is displayed (left) as a function of the two frequencies ω_{s1} and ω_{s2} for $T = 500\,\mathrm{fs}$, and (right) as a function of the Raman frequency ω_{R} and time delay T for a mean frequency $(\omega_{\mathrm{s1}} + \omega_{\mathrm{s2}})/2 = 374\,\mathrm{THz}$. The colorbar in the left panel was chosen to highlight the weaker peaks appearing in the top-right quadrant.

$S_{\mathrm{ISRS}}(\omega_{\mathrm{s2}}, T)$, independent of the value of ω_{s2}. On the other hand, the signal is determined by the action of the stochastic probe pulse at frequencies ω_{s2} and $\omega_{\mathrm{s2}} \pm \Omega$. For cross-correlations to appear, it is necessary that also these frequencies lie above the threshold frequency ω_{th}. In Fig. S9, three peaks can be distinguished. In contrast to Fig. S7, however, these peaks only appear when both contributing frequencies lie above the threshold frequency: (i) the central peak at $\omega_{\mathrm{s1}} = \omega_{\mathrm{s2}}$ is only present when both frequencies are larger than ω_{th}; (ii) the off-diagonal peak along $\omega_{\mathrm{s1}} = \omega_{\mathrm{s2}} - \Omega$ only appears if $\omega_{\mathrm{s1}} > \omega_{\mathrm{th}}$ and $\omega_{\mathrm{s2}} - \Omega > \omega_{\mathrm{th}}$; and (iii) the off-diagonal peak along $\omega_{\mathrm{s1}} = \omega_{\mathrm{s2}} + \Omega$ only appears for $\omega_{\mathrm{s1}} > \omega_{\mathrm{th}}$ and $\omega_{\mathrm{s2}} + \Omega > \omega_{\mathrm{th}}$. This creates a clear asymmetry in the cross-correlation function with respect to the Raman frequency ω_{R}, as visible in Fig. S9. Also in this case, we have assumed a small nonvanishing variance of the input and output intensities also for frequencies below ω_{th}, in order to avoid a vanishing denominator and divergences. This agrees with the experimental results, explaining the large strength of the peaks in the bottom-right quadrant of the left panel of Fig. S9 compared to the weaker peaks in the top-right quadrant.

S6. COMPARISON WITH TRADITIONAL PUMP-PROBE SPECTROSCOPY

We have performed mean-value based pump-probe measurements on the same alpha-quartz sample as a comparison to the covariance-based pump-probe spectroscopy technique. Table S1 summarizes the phonon dephasing times extracted for the three most prominent phonon modes within the pulse bandwidth used in these measurements. The mean-value and covariance-based measurements were performed one after the other, so experimental parameters could be kept consistent. The dephasing times are consistent within error margins between the two measurement techniques.

	3.9 THz	6.3 THz	13.9 THz
Covariance-based	2.67 ps	0.67 ps	1.22 ps
Mean-value	2.33 ps	0.45 ps	1.4 ps

Table S1. Phonon dephasing times measured using covariance based and mean-value based pump-probe techniques.

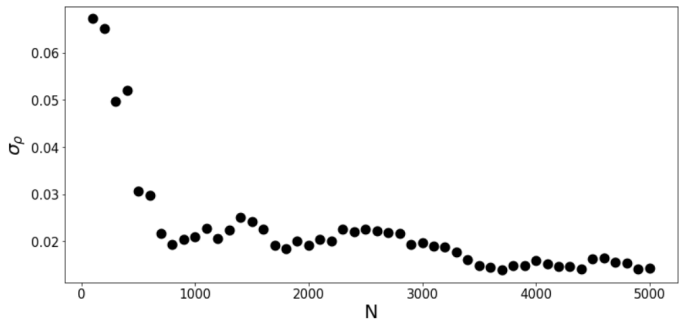

Figure S10. Standard deviation of a 15x15 pixel section of the covariance map for $\Delta T = -3\,ps$ in the quadrant where signal normally appears. This is a measure of the background due to spectrally uncorrelated noise in the detection system.

S7. UNCORRELATED BACKGROUND NOISE IN 2D CORRELATION MAPS

Spectrally uncorrelated noise introduced by the detection system (e.g. detector noise and electrical readout noise) produces a background contribution in the eventual 2D covariance maps that can obscure weak signals from the sample. However, this undesirable contribution to the measured spectra is relatively small compared to the real fluctuations in the probe pulse which contain the sample-induced correlations. In the correlation maps, the uncorrelated detection noise presents as a random signal nearly independent of ω_{OUT} and ω_{IN}, with positive and negative values distributed normally around zero. We can thus characterize the background noise level with a standard deviation of the values in areas of the covariance map where there is not signal present. This standard deviation of values decreases for increasing number of unique spectra acquired.

To quantify this effect in our measurement, we have taken the standard deviation (σ_ρ) of all points in a 15x15 pixel box within the lower right quadrant of the cross-correlation map (as indicated by the black dashed box in fig. 1c in the main text) for a single pump-probe delay. A pump-probe delay of -3 ps was chosen to ensure no signal was present. In Fig. S10 σ_ρ is plotted as a function of the number of unique spectra included in the calculation (N), showing a rapid decrease in σ_ρ below $N = 800$, followed by a slower decrease thereafter, tangentially approaching $\sigma_\rho = 0.01$. A thorough analysis of this noise is beyond the scope of this work, but it demonstrates that the signal (which has peak values of $\rho = \pm 0.1 - 0.2$) can be clearly resolved even with relatively low N.

A related question is how ρ can be connected to physically relevant quantities measured in traditional mean-value based experiments, such as $\Delta T/T$. Unfortunately there are intrinsic differences between the measurement techniques that hinder a direct connection. For example, ρ depends on two frequencies, whereas $\Delta T/T$ is measured at only a single frequency. Furthermore, the degree of correlation induced by a given signal depends on experimental parameters such as the amplitude and spectral width of the fluctuations introduced in the probe, and over what fraction of the probe bandwidth they are applied.

With that said, we have attempted to make a comparison between the results reported here with mean-value $\Delta T/T$ measurements performed on the same sample in similar conditions. In this case, we find that a correlation value of $\rho = 0.1$ is comparable to $\Delta T/T \approx 0.01$, but stress that this is not a universal relationship, and future work should be undertaken to understand in what circumstances ρ can be linked to $\Delta T/T$ or $\Delta R/R$ in a quantitative way.

[1] K. E. Dorfman, B. P. Fingerhut, and S. Mukamel, Time-resolved broadband Raman spectroscopies: A unified six-wave-mixing representation, J. Chem. Phys. **139**, 124113 (2013).
[2] C. A. Marx, U. Harbola, and S. Mukamel, Nonlinear optical spectroscopy of single, few, and many molecules: Nonequilibrium Green's function QED approach, Phys. Rev. A **77**, 022110 (2008).
[3] G. Fumero, G. Batignani, K. E. Dorfman, S. Mukamel, and T. Scopigno, On the Resolution Limit of Femtosecond Stimulated Raman Spectroscopy: Modelling Fifth-Order Signals with Overlapping Pulses, ChemPhysChem **16**, 3438 (2015).

[4] S. M. Cavaletto, D. Keefer, and S. Mukamel, High temporal and spectral resolution of stimulated x-ray Raman signals with stochastic free-electron-laser pulses, Phys. Rev. X **11**, 011029 (2021).
[5] N. Rohringer and R. Santra, X-ray nonlinear optical processes using a self-amplified spontaneous emission free-electron laser, Phys. Rev. A **76**, 033416 (2007).
[6] T. Pfeifer, Y. Jiang, S. Düsterer, R. Moshammer, and J. Ullrich, Partial-coherence method to model experimental free-electron laser pulse statistics, Opt. Lett. **35**, 3441 (2010).
[7] S. M. Cavaletto, C. Buth, Z. Harman, E. P. Kanter, S. H. Southworth, L. Young, and C. H. Keitel, Resonance fluorescence in ultrafast and intense x-ray free-electron-laser pulses, Phys. Rev. A **86**, 033402 (2012).